

# Chemical Science

Accepted Manuscript

This article can be cited before page numbers have been issued, to do this please use: Y. Yan and Q. Yuan, *Chem. Sci.*, 2026, DOI: 10.1039/D6SC02374F.



This is an Accepted Manuscript, which has been through the Royal Society of Chemistry peer review process and has been accepted for publication.

Accepted Manuscripts are published online shortly after acceptance, before technical editing, formatting and proof reading. Using this free service, authors can make their results available to the community, in citable form, before we publish the edited article. We will replace this Accepted Manuscript with the edited and formatted Advance Article as soon as it is available.

You can find more information about Accepted Manuscripts in the [Information for Authors](#).

Please note that technical editing may introduce minor changes to the text and/or graphics, which may alter content. The journal's standard [Terms & Conditions](#) and the [Ethical guidelines](#) still apply. In no event shall the Royal Society of Chemistry be held responsible for any errors or omissions in this Accepted Manuscript or any consequences arising from the use of any information it contains.

## Perspective

**Synergistic Mechanisms of Metal-Based Supports in Ru-Based HER Catalysts: From Dimensional Perspective to Metal-Support Interaction Engineering**Ya Yan,<sup>a</sup> and Qiang Yuan\*<sup>a</sup>Received 00th January 20xx,  
Accepted 00th January 20xx

DOI: 10.1039/x0xx00000x

The transition to a sustainable energy system requires efficient renewable energy conversion and storage technologies. Green hydrogen produced through water electrolysis offers a promising solution for storing intermittent renewable energy as a clean chemical fuel. The core of this technology is the hydrogen evolution reaction (HER), the efficiency of which fundamentally depends on the design of the catalyst that promotes it. In recent years, supported metal-based catalysts have garnered significant attention due to their unique electronic structures and synergistic catalytic effects. This review summarizes the research progress on metal-based support-loaded Ru-based catalysts for the HER, beginning with an examination of the intrinsic characteristics of these metal-based supports. Importantly, this review systematically categorizes representative metal-based support materials according to their dimensionality (0D, 1D, 2D, and 3D) and provides an in-depth discussion on the regulatory mechanisms of metal-support interactions (MSI) influenced by supports of different dimensions—a unique perspective that distinguishes this work from existing reviews. Finally, the challenges and future development directions for metal-based support-loaded catalysts in HER applications are thoroughly discussed. This review aims to provide theoretical guidance for designing next-generation high-performance HER electrocatalysts for sustainable energy applications.

**1 Introduction**

Hydrogen is increasingly recognized not only as a clean energy carrier with a high gravimetric energy density of ~120 MJ/kg and zero-carbon emissions, but also as a versatile feedstock for the chemical and metallurgical industries. It enables the safer production, storage, and transportation of value-added chemicals, including green ammonia (17.6 wt.% H<sub>2</sub> capacity, 11.5 MJ/L volumetric energy density), methanol (12.5 wt.% H<sub>2</sub> capacity, 15.7 MJ/L volumetric energy density), and hydrazine hydrate (8.0 wt.% H<sub>2</sub> capacity, 9.9 MJ/L volumetric energy density).<sup>1-4</sup> In this context, water electrolysis has emerged as a key route toward large-scale hydrogen production, offering a pathway to decarbonize both the energy and chemical sectors.<sup>5-8</sup> However, the hydrogen evolution reaction, as the core half-reaction in the electrolysis process, suffers from sluggish kinetics that severely limits the overall energy conversion efficiency.<sup>9,10</sup> Although platinum-based catalysts exhibit optimal hydrogen adsorption free energy, their high cost and scarcity restrict widespread adoption. Among candidate metals for platinum replacement, ruthenium (Ru) stands out. This is due not only to its substantial cost advantage, but also to the tunability arising from its unique electronic structure.

Compared with platinum, the 4d orbitals of Ru feature a higher density of electronic states, providing greater tunability in hydrogen adsorption behaviour. Thus, through support effects or coordination environment engineering, Ru-based catalytic performance could potentially exceed that of Pt-based systems. Moreover, Ru exhibits superior water dissociation capability under alkaline conditions, a feature that not only enables efficient hydrogen evolution but also offers a new avenue to overcome the kinetic limitations of alkaline water electrolysis.<sup>11-13</sup> Nevertheless, the practical application of Ru still faces bottlenecks. Its excessively strong hydrogen adsorption impedes intermediate desorption, while its high surface energy renders the active species prone to agglomeration and deactivation during reactions.<sup>14-16</sup> The essence of both issues points to the need for precise modulation of the electronic structure of Ru. Loading Ru onto appropriate supports and utilizing metal-support interactions to optimize its electronic states proves effective in overcoming these limitations.<sup>17-19</sup>

Supports are not inert scaffolds. Their intrinsic properties profoundly influence the catalytic behaviour of the supported metals. Unlike extensively studied carbon-based materials, metal-based supports are not merely passive but possess intrinsic catalytic activity and can form metal-metal interactions with Ru species. This offers a unique platform for tailoring electronic structures and reaction pathways.<sup>20-22</sup> More importantly, the dimensional characteristics of metal-based supports, which range from zero-dimensional (0D) to three-dimensional (3D), play a decisive role in determining their

<sup>a</sup> State Key Laboratory of Green Pesticide, Center for R&D of Fine Chemicals, College of Chemistry and Chemical Engineering, Guizhou University, Guiyang, Guizhou Province 550025, PR China.  
E-mail: qyuan@gzu.edu.cn



physicochemical properties. These characteristics also directly govern the dispersion state of Ru species, the efficiency of interfacial charge transfer, and the realization of synergistic catalytic mechanisms.<sup>23-25</sup> 0D metal nanoparticles exploit quantum size effects and atomically dispersed anchoring sites to achieve fine modulation of the electronic states of Ru through interfacial coupling.<sup>26-28</sup> One-dimensional (1D) metal nanowires utilize axial conductive pathways and high aspect ratios to facilitate rapid charge transport while exposing abundant active edges.<sup>29-31</sup> Two-dimensional (2D) metal-based materials, such as transition metal dichalcogenides and MXenes, with their atomic-level thickness and tunable surface functional groups, provide an ideal platform for constructing strongly coupled interfaces through face-to-face contact.<sup>32-34</sup> 3D metal frameworks, through interconnected hierarchical pore structures, synergistically optimize mass diffusion and electron conduction, providing a structural basis for stable operation under high current densities.<sup>35-37</sup>

A series of reviews have systematically summarized Ru-based hydrogen evolution catalysts, primarily focusing on strategies

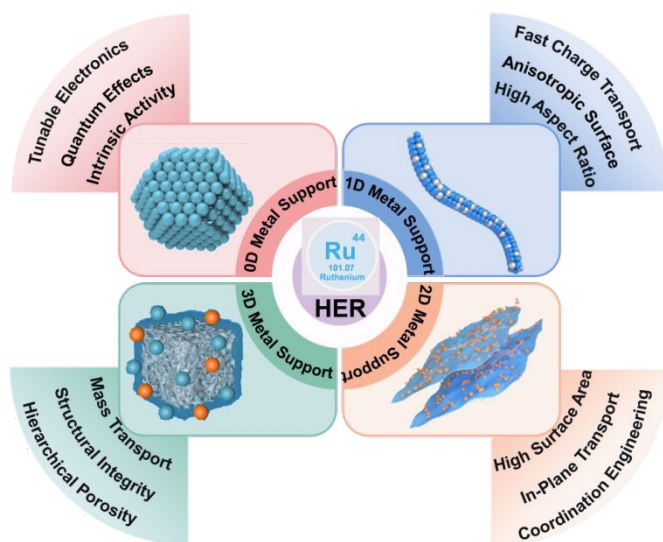


Figure 1 Dimensional engineering for metal materials in hydrogen evolution reaction.

to modulate the active centers, including nanoparticle size control, morphology engineering, crystal facet and alloy design,<sup>38-43</sup> as well as the development of novel Ru-based compounds such as sulfides and phosphides.<sup>44-47</sup> However, systematic analyses regarding supports, particularly metal-based supports, remain scarce. More critically, the core question of how support dimensionality influences catalytic performance through metal-support interactions remains to be fully elucidated. In fact, the same metal-based material can exhibit distinctly different modulation mechanisms for the electronic states of Ru, depending on whether it is in 0D, 1D, 2D, or 3D form. This concept represents a fundamental principle in the rational design of efficient catalysts, highlighting the importance of morphological control in modulating catalytic performance.

Herein, we present a dimension-dependent perspective ranging from 0D to 3D to elucidate how metal-support interactions govern the HER performance of Ru-based catalysts. In this framework, the unique advantages of Ru, including its tunable electronic states and superior water dissociation capability, are integrated with the intrinsic properties of metal-based supports. The discussion is further extended to the operando evolution of Ru species, and device-level performance is evaluated to guide the selection of suitable support dimensions for practical applications. By integrating insights from operando characterization and device-level evaluation, a more comprehensive foundation for the rational design of Ru-based catalysts is aimed to be provided by this review.

## 2 Mechanism Aspect

### 2.1 Mechanism of HER

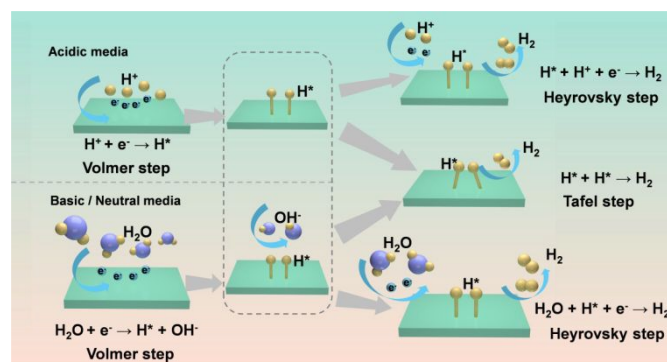


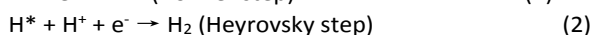
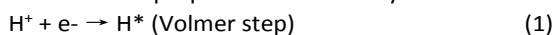
Figure 2 Schematic depiction of the detailed HER pathway.

As a key cathodic reaction in electrocatalytic water splitting, HER operates across diverse electrolyte conditions, including acidic, alkaline, and neutral media.<sup>48,49</sup> The reaction typically follows either the Volmer-Heyrovsky or Volmer-Tafel mechanism, both of which involve the adsorption and desorption of hydrogen (Figure 2).<sup>50,51</sup> The rate of the HER is influenced by factors such as the chosen reaction pathway, the proton source, and the surface properties of the catalyst.<sup>49,52</sup> Therefore, understanding the HER mechanisms under different electrolyte conditions is essential for the development of efficient catalysts.

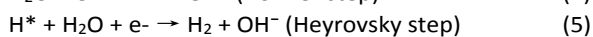
In acidic media, the HER typically proceeds through three fundamental steps. The Volmer step describes the initial stage, wherein protons ( $H^+$ ) in the electrolyte are reduced on the catalyst surface, producing adsorbed hydrogen ( $H^*$ ) (Equation 1).<sup>53</sup> In the next stage, the adsorbed hydrogen species can proceed via either the Heyrovsky mechanism, reacting with a further proton and electron to generate molecular hydrogen (Equation 2), or the Tafel mechanism, involving direct recombination of two  $H^*$  adatoms (Equation 3).<sup>54</sup> Accordingly, the overall reaction mechanism of HER and the identification of its rate-determining step are closely associated with factors



such as the electrolyte environment, surface coverage of  $H^*$ , and the electronic properties of the catalyst.<sup>55,56</sup>



In alkaline or neutral media, the absence of free protons ( $H^+$ ) in solution renders water molecules the primary proton source for the HER, thereby exerting a substantial influence on the reaction pathway and kinetic behavior.<sup>54</sup> Although HER still proceeds through three elementary steps, the Volmer step involves the dissociation of water molecules, resulting in a comparatively sluggish reaction rate.<sup>53</sup> Specifically, water molecules first adsorb onto the catalyst surface and acquire electrons, yielding adsorbed hydrogen ( $H^*$ ) alongside hydroxide ions ( $OH^-$ ) (Equation 4). Subsequently, the adsorbed hydrogen can react with an additional water molecule and a further electron via the Heyrovsky route to produce  $H_2$  and  $OH^-$  (Equation 5). Alternatively, two neighboring  $H^*$  species may combine directly through the Tafel pathway to form  $H_2$  (Equation 6).



## 2.2 Theoretical Descriptors for HER

Theoretical descriptors are the key bridge connecting the microelectronic structure of catalysts with the macro HER performance. By calculating and simulating these parameters, the physical and chemical nature of catalytic activity can be revealed, and a basis can be provided for the rational design of efficient catalysts. Among these descriptors, the hydrogen adsorption free energy ( $\Delta G_{H^*}$ ) is the most crucial thermodynamic parameter, describing the adsorption strength of hydrogen intermediates on the catalyst surface.<sup>57</sup> According to the Sabatier principle, an ideal catalyst should have a moderate adsorption capacity for hydrogen, i.e.  $\Delta G_{H^*} \approx 0$  eV (Figure 3a).<sup>58</sup> Adsorption that is too strong impedes hydrogen desorption, whereas overly weak adsorption fails to activate hydrogen effectively. By correlating the experimentally measured exchange current density with the theoretical  $\Delta G_{H^*}$ , a classic volcano diagram relationship can be obtained, whose vertices usually correspond to high-performance catalysts such as Pt, intuitively revealing the design principle of approaching zero  $\Delta G_{H^*}$  by adjusting the electronic structure of the material (Figure 3b).<sup>59,60</sup> However, in actual electrochemical environments,  $\Delta G_{H^*}$  is dynamically influenced by various factors, such as electrode potential, solvation effect, solution pH value, and hydrogen coverage, which may significantly regulate adsorption energy.<sup>49</sup> The electrode potential changes the adsorption energy by adjusting the surface charge state, which is particularly significant in 2D materials. The solvation effect stabilizes or weakens the adsorption of hydrogen intermediates through the interaction between water molecules and ions in the electrolyte. The pH value of the solution profoundly affects the adsorption strength and reaction pathway by altering the structure of the proton source ( $H_3O^+$  or  $H_2O$ ) and interface water molecules. The hydrogen coverage determines the

interaction between adsorption sites, and the repulsion effect under high coverage usually increases  $\Delta G_{H^*}$ . In summary,  $\Delta G_{H^*}$  in practical electrochemical environments is governed by a complex interplay of these factors rather than an intrinsic material property alone.

However, under alkaline or neutral conditions where the reaction begins with the dissociation of water molecules, relying solely on  $\Delta G_{H^*}$  is insufficient to fully describe the kinetic behaviour of catalysts. Given this, the water dissociation energy barrier ( $\Delta G_{H_2O}$ ) emerges as another critical theoretical descriptor. This parameter quantifies the facility with which a catalyst activates the H–OH bond, directly determining the rate of initial proton supply in alkaline systems (Figure 3c).<sup>61–63</sup> The water dissociation process begins with the adsorption of water molecules. Water molecules typically coordinate with metal surface sites via the oxygen atom, forming the adsorbed state  $H_2O^*$ . This initial adsorption configuration directly influences the facility of subsequent dissociation.<sup>62</sup> Xiang et al. investigated Au– $H_2O$ –Au single-molecule junctions and elucidated the influence of water adsorption orientation on its electronic coupling strength. In the parallel adsorption configuration, the molecular plane of water is oriented parallel to the metal surface, allowing the oxygen atom to form effective coordination with the metal site. By contrast, the perpendicular adsorption configuration, in which the two hydrogen atoms point either toward or away from the surface, exhibits substantially weaker electronic coupling.<sup>64</sup> This finding



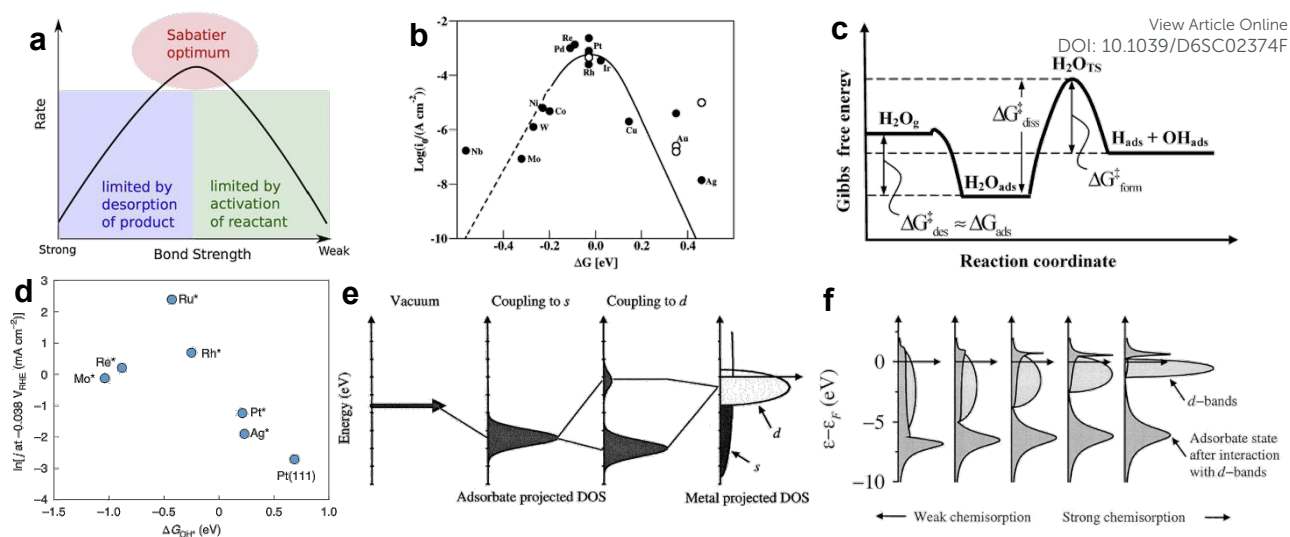


Figure 3 a) Schematic depiction of the Sabatier principle in qualitative terms.<sup>58</sup> Copyright©2015, Elsevier. b) A volcano plot.<sup>60</sup> Copyright©2010, American Chemical Society. c) Simplified potential energy profiles for water dissociation over various transition metal and noble metal dimers.<sup>63</sup> Copyright© 2009 American Chemical Society. d) Natural logarithm of experimentally measured hydrogen evolution rates on Pt (553) and Pt (553) with step-edge adsorbed species (Mo, Re, Ru, Rh, and Ag) at high coverage, plotted against DFT-calculated hydroxide adsorption free energies at 0 V vs. RHE.<sup>65</sup> Copyright©2020, Springer Nature. e) Schematic depiction of chemical bond formation between an adsorbate valence level and the s and d orbitals of a transition metal surface.<sup>69</sup> Copyright©2005, Springer Science. f) Projected local density of states for an adsorbate state interacting with surface d bands.<sup>70</sup> Copyright©2000, Academic Press.

implies that parallel-adsorbed water molecules are more readily polarized by the surface, with their O–H bonds elongated and weakened due to strong interaction with the surface, potentially leading to a lower water dissociation energy barrier. More critically, the ability of the catalyst surface to polarize the H–OH bond dictates the magnitude of the water dissociation energy barrier. Specifically, the local electron density at the metal surface influences the charge distribution within the water molecule. If the surface can effectively attract the lone pair electrons on the O atom while simultaneously repelling the H atoms, the O–H bond becomes polarized and elongated, its bond strength diminishes, and dissociation proceeds more readily. Zeinalipour-Yazdi et al. performed DFT calculations on transition metal dimers and revealed significant differences in the ability of various metals to stabilize the OH intermediate. For instance, the water dissociation free energy barrier for Fe<sub>2</sub> is as low as 0.27 eV, whereas that for Ni<sub>2</sub> reaches as high as 1.13–1.15 eV. This discrepancy originates precisely from the distinct capabilities of these two metals in stabilizing the OH\* intermediate.<sup>63</sup>

The adsorption free energy of the hydroxyl intermediate (OH) generated from water dissociation, denoted as  $\Delta G_{\text{OH}}$ , exerts a dual regulatory role on reaction kinetics. On one hand, moderate OH adsorption helps stabilize the transition state of water dissociation. At the moment of O–H bond cleavage, if the incipient OH fragment is appropriately anchored by the surface, the energy of the overall transition state structure decreases, thereby lowering the dissociation energy barrier (Figure 3d).<sup>65</sup> This effectively provides a pivot point for the reaction pathway, rendering water dissociation more energetically favourable. On the other hand, if  $\Delta G_{\text{OH}}$  is too negative—indicating excessively strong OH adsorption—the OH species cannot readily desorb from active sites, gradually accumulating and poisoning the surface, thereby hindering subsequent water adsorption and

dissociation. Conversely, if  $\Delta G_{\text{OH}}$  is too positive, reflecting overly weak adsorption, the transition state of water dissociation lacks stabilization, leading to an increased energy barrier. Therefore, an ideal alkaline HER catalyst requires synergistic optimization among  $\Delta G_{\text{H}}$ ,  $\Delta G_{\text{H}_2\text{O}}$ , and  $\Delta G_{\text{OH}}$ —achieving kinetic matching among the three steps of water dissociation, H generation, and H<sub>2</sub> desorption—wherein the strength of OH\* adsorption serves as the critical regulatory valve connecting water dissociation with site regeneration.

From a more fundamental electronic structure perspective, the regulation of the adsorption behaviours can be understood through the d-band center theory.<sup>66,67</sup> This theory originates from the chemical model of adsorption on transition metal surfaces: upon hybridization between the adsorbate's bonding orbital and the metal d-band, bonding and antibonding states are formed, and the degree of filling of the antibonding states dictates the adsorption strength (Figure 3e, f).<sup>68–70</sup> The position of the d-band center ( $\epsilon_d$ ) relative to the Fermi level serves as the core parameter describing this effect. An upward shift of the d-band center raises the energy of the antibonding states, reducing their occupancy and thus strengthening adsorption. Conversely, a downward shift lowers the energy of the antibonding states, increasing their occupancy and weakening adsorption. Based on this mechanism, tuning the d-band center of catalysts through approaches such as alloying, strain engineering, or heterostructure construction enables targeted regulation of  $\Delta G_{\text{H}}$ ,  $\Delta G_{\text{OH}}$ , and  $\Delta G_{\text{H}_2\text{O}}$ .<sup>71</sup> A downward shift of the d-band center, for instance, is typically induced by compressive strain, weakening adsorption, whereas the opposite effect arises from tensile strain;<sup>72</sup> charge transfer at heterointerfaces can also modulate the d-band position by altering the local electron density.<sup>73</sup> Therefore, as a fundamental electronic descriptor, the d-band center offers a theoretical foundation for



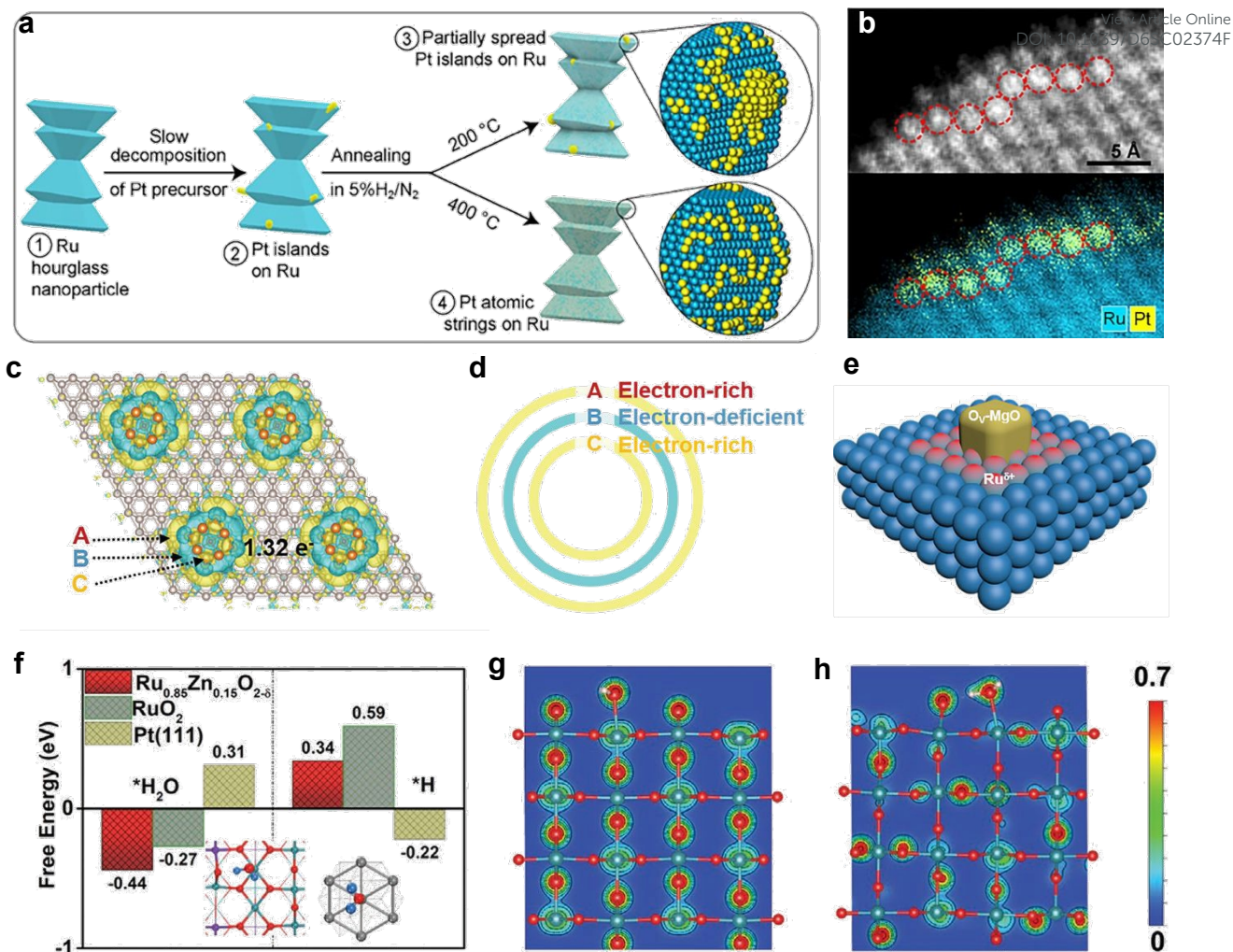


Figure 4 a) Schematic illustration of the preparation of hourglass-shaped Ru nanoparticles decorated with Pt islands, partially spread islands, and Pt atomic strings, b) Atomic-resolution STEM image and overlay EDX map of Pt and Ru showing a string-like pattern of Pt atoms on a Ru nanoparticle surface.<sup>83</sup> Copyright©2025, Wiley-VCH. c) Charge density difference of MgO-Ru. d) The onion-like charge distribution diagram of Ru atoms around MgO. e) Illustration image of MgO<sub>x</sub>-Ru system.<sup>88</sup> Copyright©2025, Wiley-VCH. f) The calculated adsorption free energy for H<sub>2</sub>O and H adsorbed on Ru<sub>0.85</sub>Zn<sub>0.15</sub>O<sub>2.6</sub>, RuO<sub>2</sub> (110), and Pt (111) surfaces, respectively. The charge density distribution of the H<sub>2</sub>O adsorbed on the (110) surface of g) RuO<sub>2</sub> and h) Ru<sub>0.85</sub>Zn<sub>0.15</sub>O<sub>2.6</sub>.<sup>89</sup> Copyright©2023, Wiley-VCH.

rationally designing high-performance catalysts through the lens of electronic structure.

### 3 Dimensional insights into metal substrates

#### 3.1 0D metal-based supports

0D metal-based supports refer to metal materials that are confined to the nanoscale in all three spatial dimensions. In contrast to carbon-based supports, 0D metal supports inherently exhibit catalytic activity, where the metal-metal interactions with Ru species enable the modulation of electronic structures and optimizing of reaction pathways.<sup>74-77</sup> The quantum size effects of these materials confer tunability to their electronic structures,<sup>78</sup> while atomically dispersed metal sites enhance interfacial contact.<sup>79</sup> Typical 0D metal-based supports for hydrogen evolution catalysts include nanoparticles, nanoclusters, and nanocrystals.

**3.1.1 Metal nanoparticles.** Nanoparticles, as an important form of 0D metal-based support materials, offer a high specific surface area and abundant surface-active sites, making them a focal point in electrocatalysis research.<sup>80,81</sup> As catalyst supports, 0D structures facilitate the uniform dispersion of active components while enabling modulation of their surface electronic structures through size effects, thereby offering substantial tunability for enhanced catalytic performance.<sup>82</sup> However, achieving efficient water dissociation kinetics, optimized hydrogen adsorption free energy, and long-term operational stability under alkaline hydrogen evolution reaction conditions remains a core focus of current research. At present, compositional regulation at the atomic scale has proven to be an effective strategy. Li et al. constructed a thermodynamically stable atomic string structure by regulating the distribution of Pt atoms on the surface of Ru particles, which involves guiding the chain-like growth of Pt atoms on the Ru surface under a controlled environment. In this architecture, Pt-Pt sites are



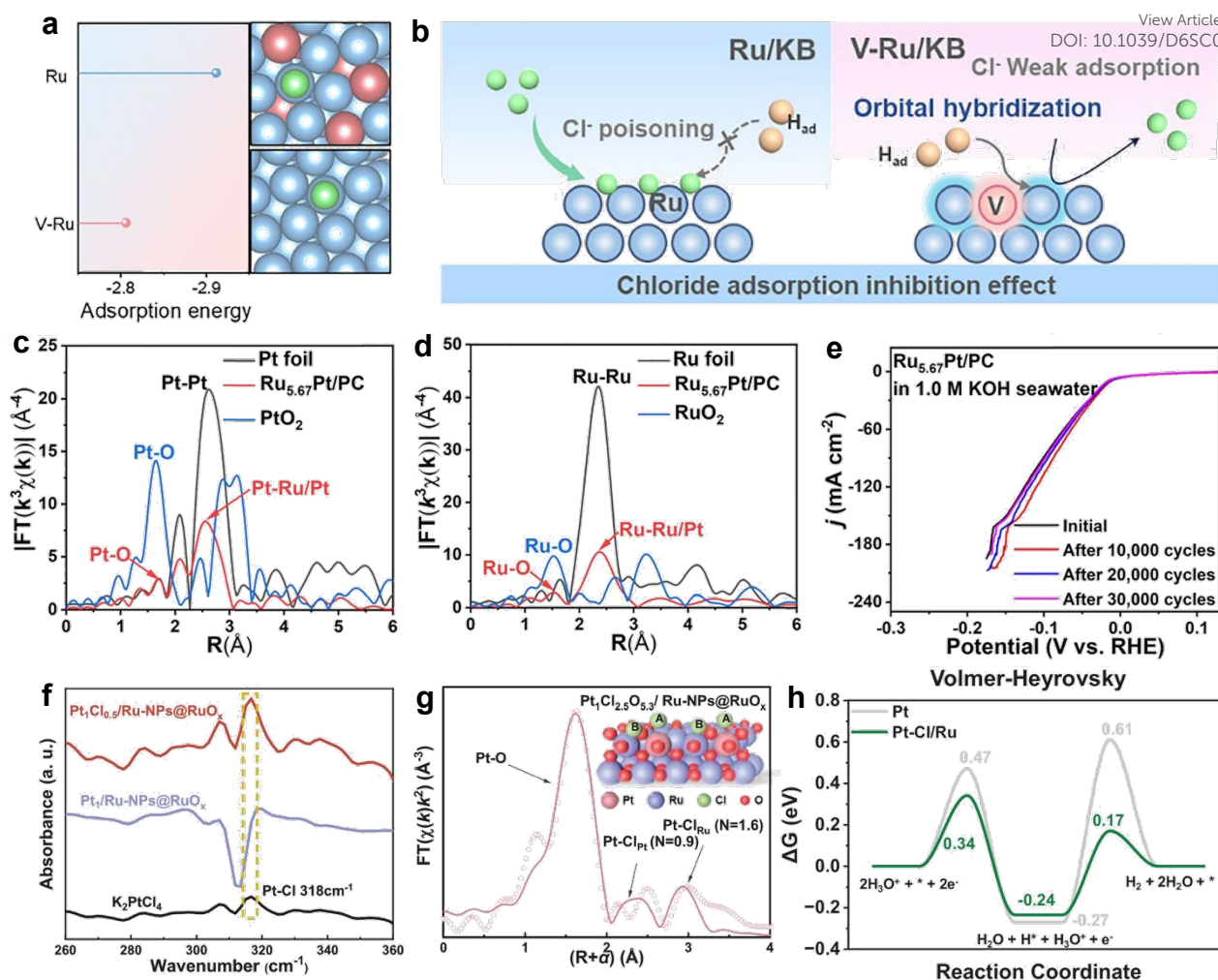


Figure 5 a) Bader charge analysis of V-Ru/KB. b) Illustration of the resistance Cl<sup>-</sup> corrosion mechanism.<sup>92</sup> Copyright©2025, Wiley-VCH. c) Corresponding FT-EXAFS curves of the Pt L<sub>3</sub>-edge and d) Ru K-edge for Ru<sub>5.67</sub>Pt/PC. e) LSV curves of Ru<sub>5.67</sub>Pt/PC before and after 30 000 CV potential cycles.<sup>94</sup> Copyright©2024, The Royal Society of Chemistry. e) IR spectra for the Pt<sub>1</sub>Cl<sub>0.5</sub>/Ru-NPs@RuO<sub>x</sub>, Pt<sub>1</sub>/Ru-NPs@RuO<sub>x</sub>, and K<sub>2</sub>PtCl<sub>6</sub>. f) Pt L<sub>3</sub>-edge EXAFS and corresponding curve fit for the Pt<sub>1</sub>Cl<sub>0.5</sub>/Ru-NPs@RuO<sub>x</sub>. g) the Volmer-Heyrovsky mechanism on Pt-Cl/Ru and Pt (111) at -0.02 V versus RHE and pH=0.<sup>95</sup> Copyright©2025, Wiley-VCH.

positioned in close proximity to Pt-Ru sites, generating a synergistic effect where Pt-Ru sites facilitate water dissociation and adjacent Pt-Pt sites convert the resulting H<sub>ads</sub> into H<sub>2</sub> via the Tafel mechanism, thereby enhancing the alkaline HER performance (Figure 4a, b).<sup>83</sup>

Furthermore, modifying the charge distribution of Ru by introducing a second metal to optimize the adsorption behaviour of reaction intermediates has been extensively explored.<sup>84-87</sup> Gu et al. proposed modifying the Ru surface with Lewis acid oxide nanoparticles, specifically anchoring MgO nanoparticles onto the Ru surface to induce an onion-like charge distribution in the surrounding Ru atoms. This charge rearrangement exposes previously inactive Ru bridge sites, which become adsorption sites for H and Cl<sup>-</sup>, optimizing intermediate adsorption and addressing the issue of suppressed reaction activity in strongly alkaline and high-salinity media (Figure 4c-e).<sup>88</sup> Hou et al. presented a new regulatory strategy using Ru<sub>0.85</sub>Zn<sub>0.15</sub>O<sub>2-δ</sub> solid-solution oxide particles prepared by a molten salt method (Figure 4f-h). Theoretical calculations show that Zn incorporation distorts the local crystal structure,

activating pendant O atoms as proton acceptors and reducing the free energy of water adsorption on the surface. Therefore, the strategy of stabilizing water molecules via Zn doping effectively enhances the alkaline HER activity.<sup>89</sup>

To address the issue of catalyst corrosion caused by the overly strong adsorption of Cl<sup>-</sup> in seawater, current research has embarked on electronic structure regulation, designing various chlorine-corrosion-resistant catalysts to enhance their stability in seawater electrolysis.<sup>90,91</sup> Sun et al. employed a V-doping strategy to modulate the electronic structure of Ru particles. The introduction of V redistributes electrons around Ru, shifting its d-band center downward relative to the Fermi level. This not only optimizes the hydrogen adsorption free energy but also significantly weakens the surface adsorption of corrosive Cl<sup>-</sup>, endowing the catalyst with excellent long-term stability under seawater electrolysis conditions (Figure 5a, b).<sup>92</sup> Shen et al., on the other hand, endowed the catalyst with high hydrophilicity by constructing a structure rich in hydroxyl and borate species on the surface of Ru nanoparticles. Compared to RuO<sub>2</sub>, the d-band center of Ru-BO<sub>x</sub>-OH exhibits a negative shift relative to



the Fermi level, which significantly weakens its surface adsorption of  $\text{Cl}^-$ . This simultaneously promotes water adsorption/activation and enhances resistance to chloride ion corrosion, offering a new design strategy for seawater electrolysis.<sup>93</sup> Furthermore, Zhang et al. constructed atomic Ru-Pt dual sites by introducing Pt atoms into Ru clusters. Utilizing the electronic synergy between Pt and Ru to optimize the hydrogen adsorption energy, they achieved a high mass activity of  $10.93 \text{ A mg}_{\text{Pt}}^{-1}$  and excellent stability over 30,000 cycles in alkaline seawater (Figure 5c-e).<sup>94</sup>

Notably, the stability issues of single-atom catalysts can also be addressed using particulate supports. Wang et al. achieved the stabilization of Pt single atoms through the synergistic effect of Cl ligands and Ru nanoparticles, where the dynamically evolving Pt-Cl-Pt coordination structure during the reaction both protects the Pt single atoms from agglomeration and modulates their electronic structure. Among these, the Pt-Cl coordination exists in two distinct environments: an axial Pt-Cl-Pt bond and a Pt-Cl-Ru bond bridging between Pt and Ru. This dual-chlorine coordination structure is fundamental to the stable anchoring of Pt single atoms on the Ru nanoparticle surface (Figure 5f-h).<sup>95</sup>

**3.1.2 Metal nanoclusters.** Metal nanoclusters, as a unique class of catalyst supports, exhibit distinctive structural advantages due to their transition size between molecules and nanoparticles. Nanoclusters can not only serve as highly active centers themselves, but the strong coupling interaction between them and the supported metal can also induce unique interfacial electronic structures, offering the potential to surpass the performance limits of traditional catalysts.<sup>96-98</sup> However, the high surface energy resulting from their ultrasmall size makes nanoclusters highly prone to agglomeration and

deactivation, while their complex surface structures also present substantial obstacles to accurately identifying and regulating active sites. The Ru/RuO<sub>2</sub> cluster system has attracted significant attention due to its unique synergistic effects. Dang et al. demonstrated through theoretical predictions combined with experimental validation that the Ru/RuO<sub>2</sub> heterogeneous interface optimizes hydrogen adsorption at the Ru sites and enhances water dissociation at the RuO<sub>2</sub> sites, effectively overcoming the kinetic limitations of water dissociation in alkaline HER.<sup>99</sup> Building on this, incorporating a third component enables charge redistribution that optimizes hydrogen adsorption, consequently enhancing the catalytic performance of the Ru/RuO<sub>2</sub> system.<sup>100-102</sup> Li et al. incorporated Mn atoms into the RuO<sub>2</sub> matrix to construct a catalyst featuring a Mn-O-Ru bridging structure, in which the asymmetric bridge configuration enables synergistic effects. In this structure, the Ru sites exhibit significantly enhanced water dissociation capability, while the bridging oxygen sites possess optimal hydrogen adsorption energy. The dissociated H\* rapidly spills over from Ru sites to adjacent oxygen sites for preferential adsorption, thereby quickly exposing active Ru sites and promoting the enrichment of water molecules at the interface. This hydrogen-spillover-bridged Volmer-Tafel mechanism synergistically ensures excellent alkaline HER performance (Figure 6a, b).<sup>103</sup> Beyond the aforementioned doping strategies, Liu et al. systematically screened various 3d transition metal-doped M-RuO<sub>2</sub> systems using density functional theory calculations and identified Ni-RuO<sub>2</sub> as the optimal candidate material. The study revealed that incorporation of Ni atoms

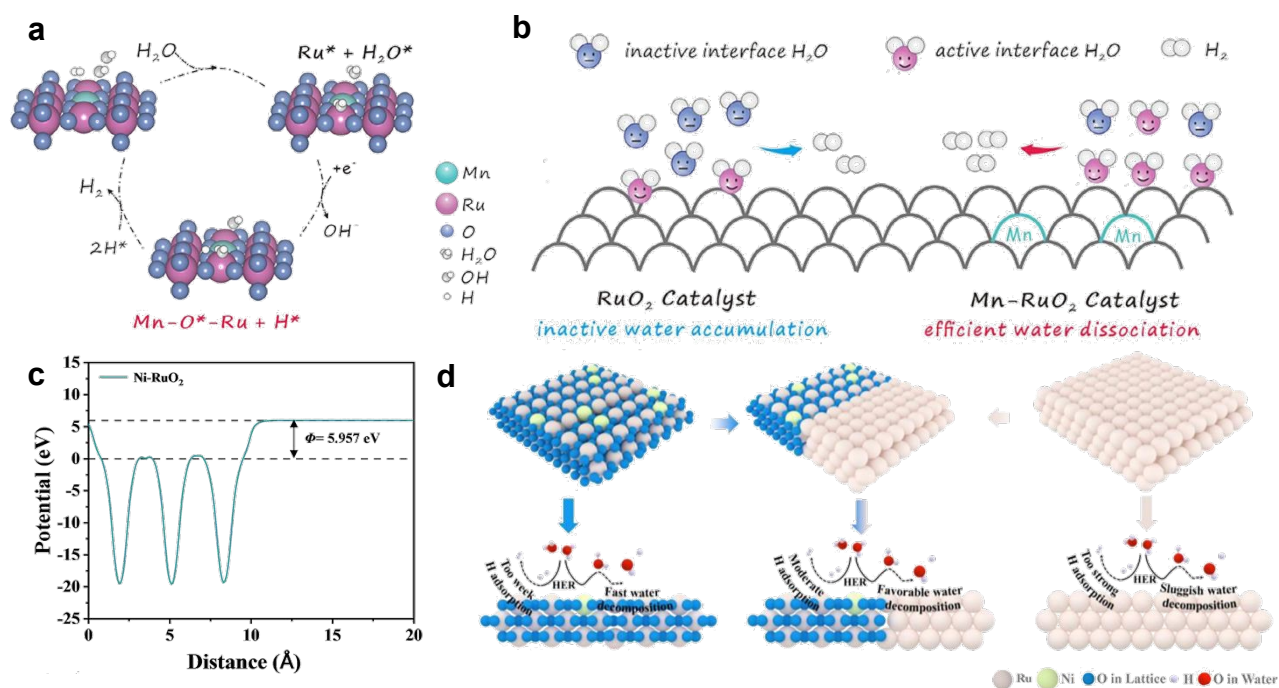


Figure 6 a) Schematic depiction of the HER catalytic pathway over the Mn-RuO<sub>2</sub> electrocatalyst. b) Schematic depiction of interfacial water dissociation on RuO<sub>2</sub> and Mn-RuO<sub>2</sub> surfaces.<sup>103</sup> Copyright©2025, Wiley-VCH. c) Work function of Ni-RuO<sub>2</sub>. d) Schematic illustration of HER mechanisms for in situ formed Ni-Ru/RuO<sub>2</sub>.<sup>104</sup> Copyright©2025, Wiley-VCH.



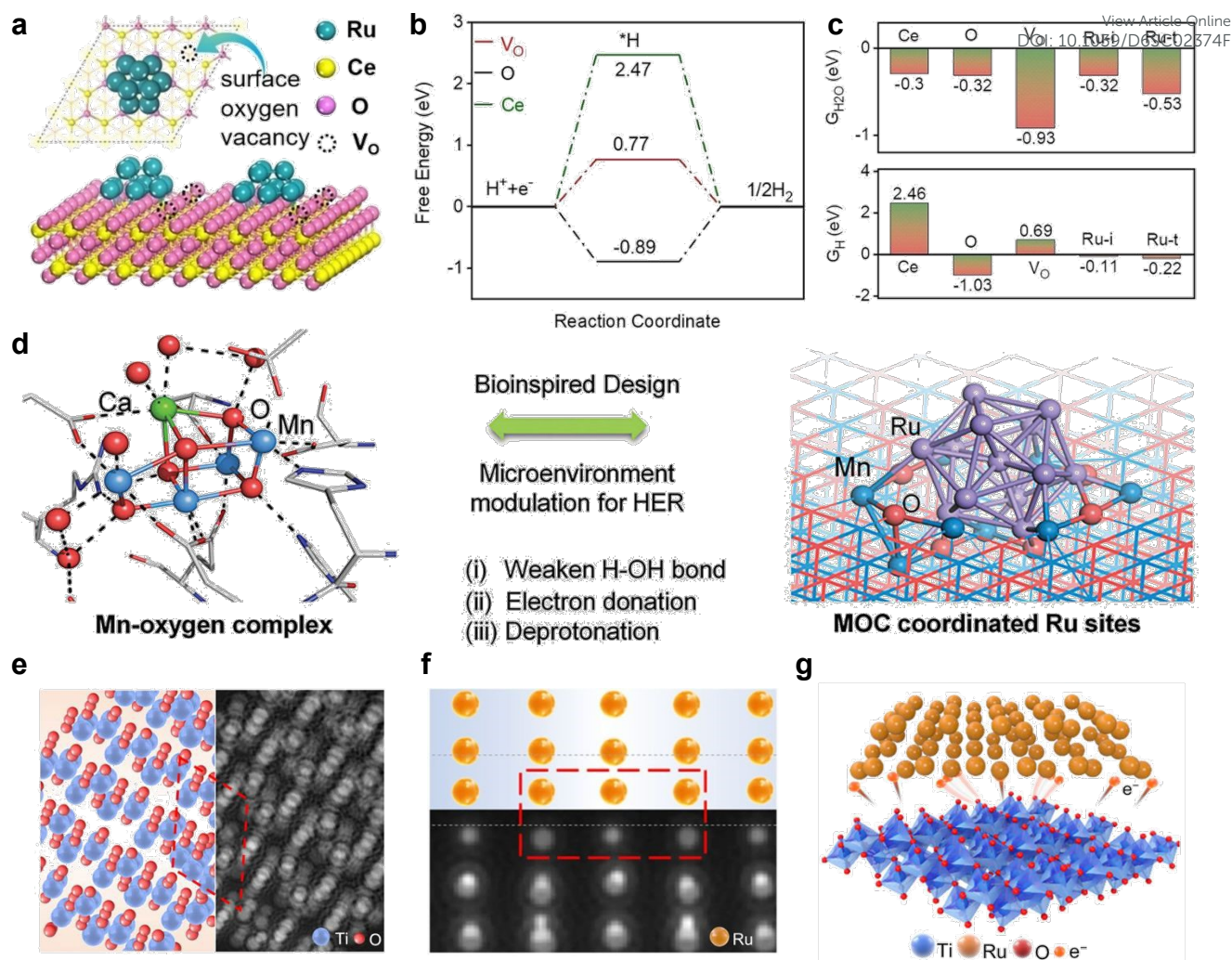


Figure 7 a) Surface O vacancy structure of Ru/ac-CeO<sub>2.6</sub>. b) Gibbs free energy profiles for H<sub>2</sub> evolution at various reaction sites on c-CeO<sub>2.6</sub>, referenced against the standard hydrogen electrode. c) Calculated adsorption free energies of H<sub>2</sub>O (G<sub>H<sub>2</sub>O</sub>) and H (G<sub>H</sub>) at various reaction sites on Ru/c-CeO<sub>2.6</sub>.<sup>107</sup> Copyright©2023, Wiley-VCH. d) Advantages of oxygen-evolving MOC and MOC-inspired design for constructing Ru sites toward water splitting.<sup>106</sup> Copyright©2023, Wiley-VCH. e, f) Schematic atomic structure and corresponding simulated HAADF-STEM images of Ti<sub>4</sub>O<sub>7</sub> and Ru in Ru/Ti<sub>4</sub>O<sub>7</sub>, respectively. g) Schematic illustration of the electronic interaction between Ti<sub>4</sub>O<sub>7</sub> and Ru.<sup>108</sup> Copyright©2024, Springer Nature.

facilitates partial reduction of RuO<sub>2</sub>, forming a Ni-Ru/RuO<sub>2</sub> interface with a pronounced built-in electric field during the electrochemical reaction. This field enhances interfacial electron transfer, which is crucial for lowering energy barriers and accelerating HER kinetics (Figure 6c, d).<sup>104</sup>

Constructing oxide cluster supports rich in oxygen vacancies enhances the metal-support interaction, which optimizes the electronic structure and adsorption energy of Ru and significantly improves hydrogen evolution reaction kinetics.<sup>105,106</sup> Qin et al. constructed an amorphous/crystalline mixed CeO<sub>2.6</sub> support and loaded highly dispersed Ru clusters on its surface. This work revealed that oxygen vacancies within the support function as Lewis acid sites, facilitating H<sub>2</sub>O adsorption and subsequent cleavage of H-OH bonds. Meanwhile, Ru clusters serve as weak Lewis base sites that promote the release of hydrogen. By designing the amorphous/crystalline mixed structure, the energy barriers of three key steps, water dissociation, hydrogen desorption, and hydroxide desorption, were simultaneously optimized,

achieving high catalytic performance (Figure 7a-c).<sup>107</sup> Inspired by natural Mn-oxygen complexes, Yang et al. used Mn-oxide compounds as supports to coordinate Ru, creating a unique deprotonated, low-oxophilic microenvironment. This structure accelerates water dissociation and promotes OH desorption, while triggering long-range hydrogen spillover under acidic conditions, thereby enhancing catalytic performance in both alkaline and acidic conditions by facilitating H<sub>2</sub>O adsorption and decomposition and assisting in OH/H<sub>2</sub> desorption at Ru sites (Figure 7d).<sup>106</sup> On the other hand, the electronic band structure and chemical stability of the support are also crucial. Zhao et al. systematically studied the interactions between Ru nanoparticles and different titanium oxide supports (TiO, Ti<sub>4</sub>O<sub>7</sub>, TiO<sub>2</sub>) and found that Ti<sub>4</sub>O<sub>7</sub>, with its distinctive electronic band structure, chemical stability and superior electrical conductivity imparted by periodically arranged oxygen vacancies, forms a sophisticated metal-support interaction with Ru through the interface Ti-O-Ru unit (Figure 7e-g).<sup>108</sup>



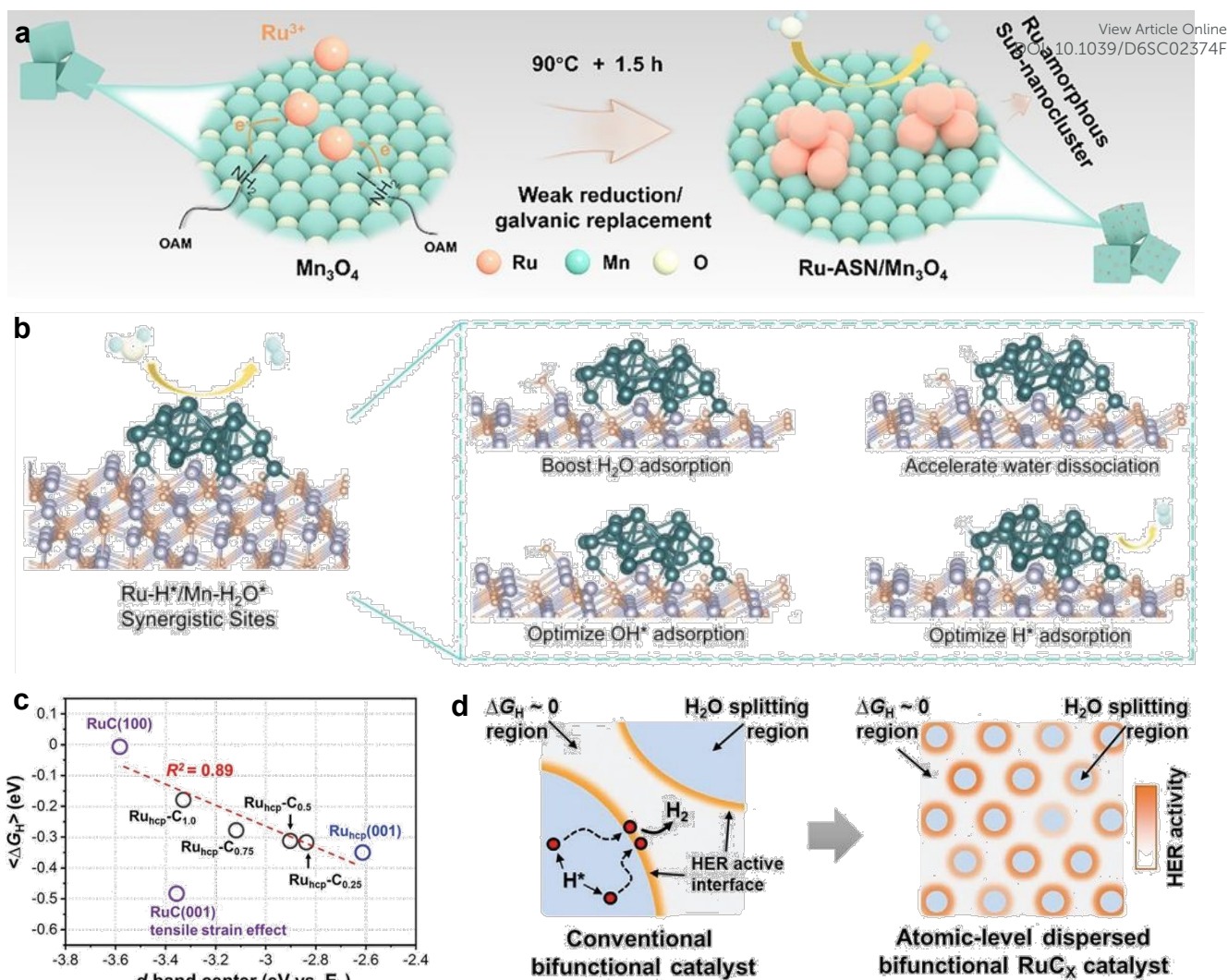


Figure 8 a) Schematic illustration of the synthesis process of Ru-ASN/Mn<sub>3</sub>O<sub>4</sub> through a surface-confined growth approach. b) The HER reaction process for the Ru-ASN/Mn<sub>3</sub>O<sub>4</sub> model under neutral conditions.<sup>115</sup> Copyright©2025, The Royal Society of Chemistry. c) Correlation between the d-band-center energy and average  $\Delta G_H$ . d) Schematic illustration depicting the atomic-scale bifunctional mechanism at the RuC<sub>x</sub> surface.<sup>116</sup> Copyright©2021, Wiley-VCH.

**3.1.3 Metal nanocrystals.** Metal nanocrystals, characterized by ordered lattice structures and abundant defect sites, can serve as ideal support platforms, enabling modulation of electronic states through phase engineering while providing precise anchoring sites for supported metals, thereby facilitating the investigation of catalytic mechanisms at the atomic scale.<sup>109,110</sup> The value of metal nanocrystals as supports lies not only in providing well-defined anchoring sites but also in their intrinsically tunable properties, rationally designable unconventional crystal phases, and dynamically evolving surface structures. These features offer extensive opportunities for understanding and optimizing Ru-based catalytic performance at the atomic scale.<sup>111–114</sup>

Inspired by the mild reducibility arising from electron transfer between Mn<sup>2+</sup>/Mn<sup>3+</sup> in Mn<sub>3</sub>O<sub>4</sub>, Wan et al. anchored amorphous Ru sub-nanoclusters onto the Mn<sub>3</sub>O<sub>4</sub> surface via a two-step low-temperature method, combining oleylamine-coordinated reduction with oleic acid protection. The study demonstrated that, upon forming a strongly coupled interface with Mn<sub>3</sub>O<sub>4</sub>, the

H adsorption free energy at Ru sites is optimized to an intermediate value, while the water dissociation barrier at Mn sites is significantly reduced. This interfacial synergy endows Ru-ASN/Mn<sub>3</sub>O<sub>4</sub> with superior HER performance under neutral conditions (Figure 8a, b).<sup>115</sup> Constructing homo- or hetero-interfaces composed of the same elements can optimize catalytic performance by tuning the interfacial electronic structure and catalytic activity.<sup>116–118</sup> Zheng et al. found that Ru nanocatalysts with a face-centered cubic structure exhibited remarkably enhanced alkaline HER performance, with this unconventional crystal structure providing more favourable adsorption energies for key reaction intermediates, thereby laying the groundwork for subsequent studies on phase-controlled catalysis.<sup>12</sup> Accordingly, Kim et al. further revealed surface reconstruction phenomena during the phase transition of Ru nanocrystals from cubic close-packed to hexagonal close-packed structures, discovering that the surface-generated ruthenium carbide phase exhibits local heterogeneity, simultaneously providing H adsorption and water dissociation sites that synergistically accelerate the alkaline HER process



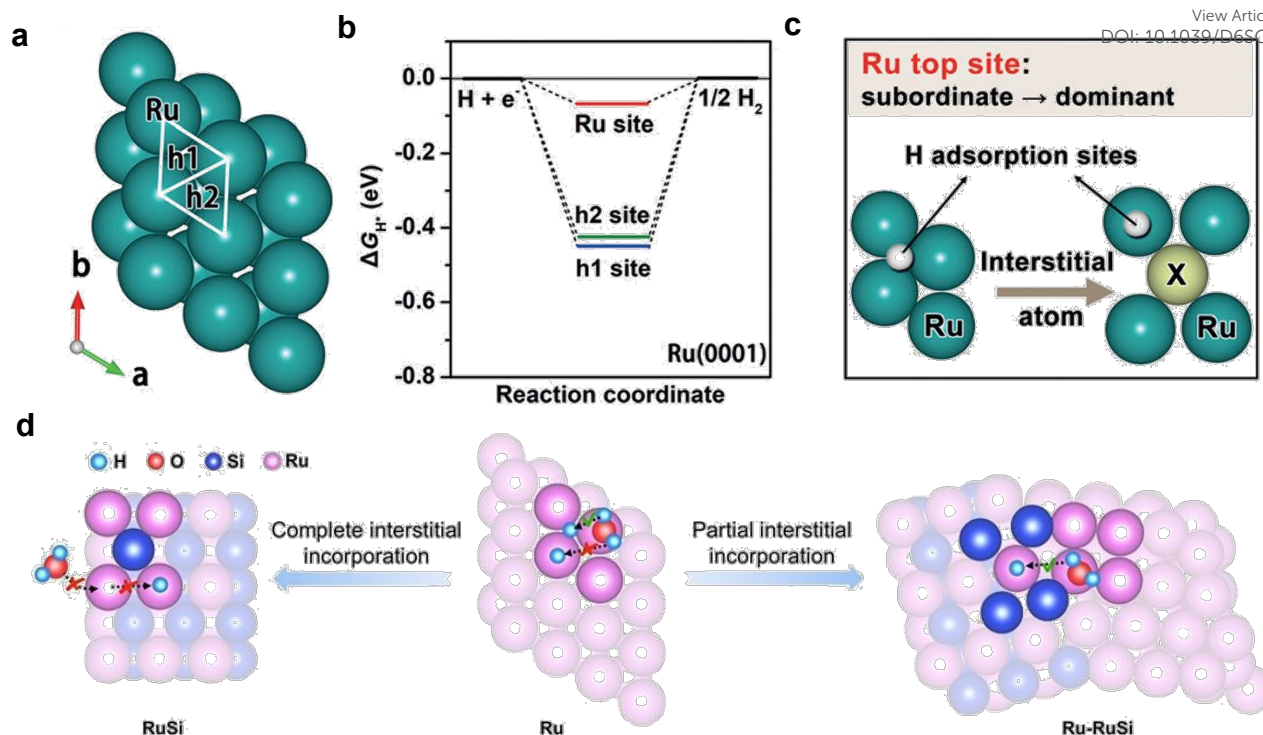
View Article Online  
DOI: 10.1039/D6SC02374F

Figure 9 a) The stable H adsorption sites and b) their calculated  $\Delta G_{H^*}$  values on the Ru (0001) surface. c) Schematic depiction of the interstitial incorporation approach for converting Ru top sites from subordinate to dominant roles.<sup>119</sup> Copyright©2019, Wiley-VCH. d) The illustration of complete interstitial incorporation strategy and partial interstitial incorporation strategy.<sup>122</sup> Copyright©2024, Wiley-VCH.

(Figure 8c, d).<sup>116</sup>

Ru species often exhibit excessively strong hydrogen adsorption, and theoretically predicted highly active sites are frequently masked or play subordinate roles under practical reaction conditions, meaning that the true catalytic center is often something other than Ru.<sup>15</sup> To transform Ru sites from implicit subordinate positions into explicit active centers, Chen et al. investigated structural regulation of RuSi at a more fundamental level and employed an interstitial atom doping strategy to elevate highly active top sites from a subordinate to a dominant role, where the enhanced activity arises from an optimized electronic structure governed by a balanced interplay between ligand and strain effects (Figure 9a-c).<sup>119</sup> Shen et al. further discovered that the true active sites for hydrogen evolution in LaRuSi are not the conventionally assumed Ru sites but rather Si sites, since Ru exhibits an unusual negative valence state and binds hydrogen too strongly, whereas the Si sites possess a hydrogen adsorption Gibbs free energy close to zero.<sup>120</sup> Building on this understanding, Zhang et al. further electrochemically activated LaRuSi<sub>3</sub>, triggering surface reconstruction that led to the formation of Ru clusters, thereby optimizing the material's charge distribution and achieving a functional division where Ru sites favour water adsorption and Si sites promote hydrogen adsorption.<sup>121</sup> Hou et al. addressed the issue of latent catalytic sites on the Ru surface by proposing a partial interstitial doping strategy. The study revealed that although the top sites on the Ru surface exhibit excellent theoretical activity, they are suppressed by excessive hydrogen adsorption at adjacent hollow sites. By partially embedding Si

atoms into the hollow sites of Ru to form a Ru-RuSi heterostructure, the Si atoms directly inhibited strong hydrogen adsorption at the hollow sites, forcing the reaction to shift towards the top sites. Meanwhile, the built-in electric field spontaneously formed at the Ru-RuSi interface bidirectionally optimized the Ru sites' ability to adsorb reaction intermediates (Figure 9d).<sup>122</sup>

Collectively, these studies demonstrate that 0D metal-based supports have evolved from passive dispersants into active electronic modulators in Ru-based catalysis. This evolution reflects a progressive pursuit of structural precision, enabling increasingly fine control over interfacial charge distribution, coordination environments, and even the identification of non-Ru active sites. The underlying rationale is consistent: the support-Ru interface serves as a tuneable chemical variable that governs catalytic behaviour through electronic perturbations. Looking forward, the central challenge lies in distilling these empirical insights into predictive design principles. Establishing correlations between the structural features of 0D supports and their electronic effects on Ru would transform current strategies into a generalizable framework for rational catalyst design.

### 3.2 1D metal-based supports

1D metal-based materials refer to linear or rod-like structures that are confined to the nanoscale (typically below 100 nm) in two dimensions while unrestricted in the third, primarily including nanowires, nanorods, and nanotubes. This



dimensional confinement imparts pronounced anisotropy and a high aspect ratio, conferring unique advantages in the design of Ru-based hydrogen evolution catalysts. The axial features provide rapid charge transport pathways to accelerate reaction kinetics, while the high aspect ratio yields a large specific surface area that exposes more active sites.<sup>123,124</sup> Moreover, the anisotropic growth characteristics allow tunability of surface facets and defect types, providing a structural basis for electronic structure modulation. Currently, 1D metal-based supports used for loading Ru-based hydrogen evolution catalysts primarily fall into two categories: metallic nanowires and metal oxide nanowires.

**3.2.1 Metallic nanowires.** Metallic nanowires, which integrate 1D geometry with multimetallic compounds, have attracted significant attention in the design of Ru-based hydrogen evolution catalysts. The 1D structure provides fast electron transport pathways and abundant surface active sites. Moreover, by modulating surface electronic structure and interfacial microenvironment through strategies such as alloying, constructing heterojunctions, or introducing foreign components, the adsorption behaviour of reaction intermediates and the reaction kinetics can be precisely

optimized. Current research focuses on further enhancing their activity and stability under alkaline conditions through compositional screening and interfacial structure design.<sup>115,125,126</sup> Zuo et al. constructed a hierarchically structured electrode using copper nanorods as the framework, with Ru-Cu nano-heterostructures decorated on their surfaces. The vertically aligned copper nanorods exhibit high electrical conductivity and porosity, providing rapid pathways for charge transfer and gas transport while maintaining high mechanical strength. The size of the surface copper clusters modulates the electronic structure of ruthenium, thereby facilitating the water dissociation step. Copper clusters grown on top of ruthenium possess a hydrogen adsorption Gibbs free energy close to zero, thereby accelerating the hydrogen evolution step.<sup>127</sup> Recently, Mao et al. proposed a strategy to address the issue of insufficient active hydrogen supply in alkaline HER by introducing soluble cations to regulate the interfacial water environment. Using electrochemically lithiated sub-2 nm RuSn<sub>0.8</sub> nanowires as the model, they found that Li incorporation into the Ru-Sn lattice lowers the water dissociation energy barrier, while some Li<sup>+</sup> ions dissolve in situ during the reaction, significantly increasing the number of

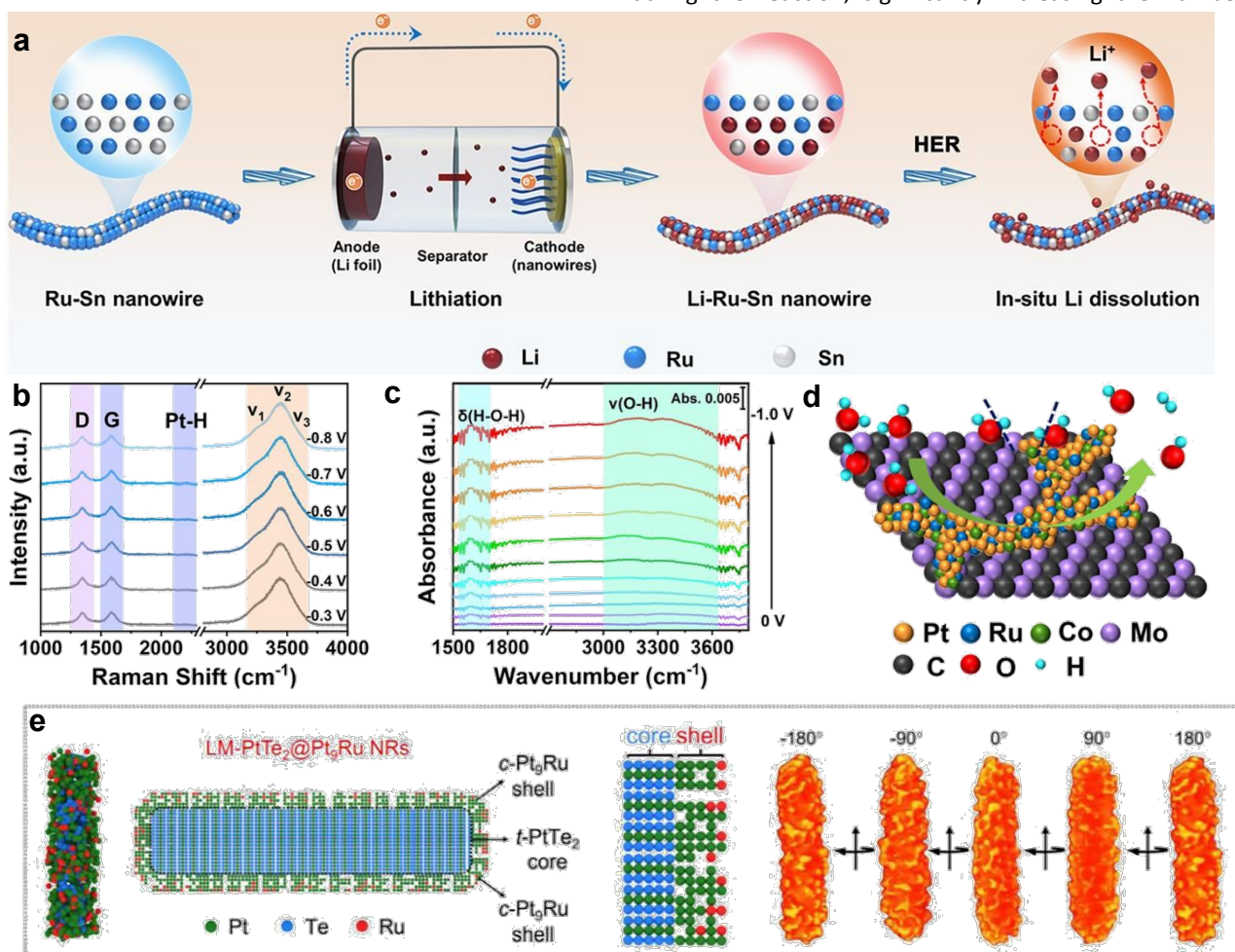


Figure 10 a) Synthesis schematic diagram of Li, Ru, and Sn nanowires.<sup>128</sup> Copyright©2025 American Chemical Society. b) In situ Raman spectra of Pt<sub>0.5</sub>Ru<sub>0.22</sub>Co<sub>0.28</sub>/Mo<sub>2</sub>C in 1.0 M PBS. c) ATR-SEIRAS spectra. d) Illustration of the proposed HER mechanism in a neutral medium.<sup>123</sup> Copyright©2025, The Royal Society of Chemistry. e) Atomic and cross-sectional models of core@shell LM-PtTe<sub>2</sub>@Pt<sub>0.5</sub>Ru NRs featuring an uneven surface morphology.<sup>133</sup> Copyright© 2025, Wiley-VCH.



interfacial water molecules and enhancing the flexibility of the hydrogen bond network, thus providing ample active protons for hydrogen production (Figure 10a).<sup>128</sup> Feng et al. constructed PtRuCo alloy nanochains and leveraged their abundant one-dimensional interfaces and inter-cluster coupling effects to optimize the free energy of hydrogen adsorption. The optimized Pt<sub>0.5</sub>Ru<sub>0.22</sub>Co<sub>0.28</sub>/Mo<sub>2</sub>C catalyst demonstrated exceptional durability over 70,000 cycles in neutral media. By employing in situ ATR-SEIRAS spectroscopy, they revealed the dynamic evolution of the interfacial water structure as a function of applied potential, providing direct evidence for understanding the mechanism of the neutral hydrogen evolution reaction. (Figure 10b-d).<sup>123</sup>

In 1D configuration, the core-shell structure allows materials with different functions to be assigned to the core and shell layers, achieving precise control through lattice mismatch and electronic interactions at the core-shell interface. Additionally, the shell layer protects the internal active components from corrosion, providing unique advantages in enhancing both activity and stability. Jiang et al. applied this concept and, by precisely controlling the oxidation temperature and time, successfully synthesized Ru@RuO<sub>2</sub> core-shell nanorods, finding that the formation of the metal-oxide interface played a key role in catalysis.<sup>129</sup> However, relying solely on the interfacial effects between metals and oxides offers limited improvement in overcoming the kinetic bottleneck of water dissociation. Researchers have further enhanced the electronic synergistic effects at the core-shell interface by constructing the core and shell as alloy systems, introducing non-metal element doping, or extending to dual-wall configurations, thereby optimizing water dissociation and hydrogen evolution kinetics through interactions among multiple components.<sup>130,131</sup> Jiang et al. took a novel approach by employing a hydrogenation strategy to synthesize hydrogen-terminated core-shell PdH@Ru nanobamboos. They prepared Pd@Ru core-shell nanorods using a hard-template method combined with epitaxial growth, then placed them in a high-pressure autoclave where in situ DMF-assisted hydrogenation introduced hydrogen atoms into the palladium core, forming the PdH@Ru structure. The hydrogen insertion not only induced tensile strain and modified the electronic structure, but the bamboo-like hollow architecture also provided abundant active sites, optimizing electron and mass diffusion in alkaline electrolytes.<sup>132</sup> Building upon the previous studies, Geng et al. noted the inevitable lattice mismatch issue in core-shell catalysts and transformed it from a disadvantage into a design tool. They constructed PtTe<sub>2</sub>@Pt<sub>x</sub>Ru core-shell nanorods with a large lattice mismatch and utilized the abundant lattice dislocations and anomalous strains induced at the interface to further optimize the surface electron distribution and the adsorption behavior of reaction intermediates (Figure 10e).<sup>133</sup>

**3.2.2 Metallic oxides nanowires.** 1D metal oxides (such as TiO<sub>2</sub>, WO<sub>3</sub>, Co<sub>3</sub>O<sub>4</sub>) are widely used as supports for ruthenium-based catalysts due to their fast electron transfer, surface oxygen vacancy anchoring sites, and metal-support interactions.<sup>31,134</sup> However, their conductivity, active sites, and stability are still

limited. Currently, performance enhancement is mainly achieved through strategies such as oxygen vacancy engineering, crystal phase regulation, heterogeneous interface construction, and optimization of metal-support interactions.

WO<sub>3</sub>, owing to its tunable crystal phases and abundant oxygen vacancies, is widely employed as support for Ru-based catalysts, particularly demonstrating unique advantages in optimizing alkaline hydrogen evolution reaction pathways via hydrogen spillover effects. Early studies focused on regulating the adsorption of reaction intermediates through multi-metal synergy.<sup>135</sup> Subsequently, researchers have progressively concentrated on exploiting the hydrogen spillover potential of WO<sub>3</sub> itself. Chen et al. constructed a proton reservoir by loading Ru nanoparticles onto oxygen-deficient WO<sub>3-x</sub>. In situ Raman spectroscopy shows that under cathodic potential, proton insertion into WO<sub>3-x</sub> coincides with the appearance of Ru–H, indicating hydrogen spillover to Ru (Figure 11a). Potential back-sweep and cyclic voltammetry further confirm that Ru facilitates reversible proton extraction from WO<sub>3-x</sub> (Figure 11b, c). This process significantly increases hydrogen coverage on Ru, shifting the rate-determining step of the hydrogen evolution reaction from sluggish water dissociation to favorable hydrogen recombination.<sup>136</sup> Building upon this foundation, researchers have further expanded the applications of WO<sub>3</sub> supports by constructing amorphous/crystalline WO<sub>3</sub>-Vo heterointerfaces or employing single-atom Ru doping strategies.<sup>137,138</sup> Recently, Xu et al. precisely synthesized WO<sub>3</sub> with different crystal phases and loaded them with Ru, discovering that hexagonal WO<sub>3</sub> provides stronger anchoring, more uniform Ru dispersion, and the smallest work function difference, thereby promoting efficient hydrogen spillover.<sup>139</sup> Zhao et al. proposed an in situ electrochemical reconstruction strategy on Ru/WO<sub>x</sub> catalysts, where the reconstruction dilutes the interfacial electron density and lowers the thermodynamic barrier for hydrogen migration, thereby generating thermoneutral RuO<sub>x</sub>/WO<sub>2</sub> interfacial sites and optimizing the hydrogen spillover pathway.<sup>140</sup>

Co<sub>3</sub>O<sub>4</sub>, with its mixed valence states (Co<sup>2+</sup>/Co<sup>3+</sup>) and abundant oxygen vacancies, not only forms strong metal-support interactions with Ru to modulate its electronic states but also participates in the water dissociation process as an active substrate, making it an ideal platform for constructing Ru-based bifunctional catalysts. The core of research on this system lies in how to utilize Co<sub>3</sub>O<sub>4</sub> to precisely modulate the local coordination environment and interfacial coupling effects of Ru to achieve synergistic catalysis. In recent years, the research focus has gradually shifted towards synergistically designing coordination and interfaces to optimize the electronic structure and reaction pathways of Ru at the atomic scale.<sup>31,141,142</sup> Wang et al. further constructed a heterostructure featuring seamless integration of an electron-enriched amorphous CoRuO<sub>x</sub> layer atop a crystalline Ru-doped Co<sub>3</sub>O<sub>4</sub> substrate. They found that this design induces a downshift in the d-band center of Ru, facilitating H<sub>2</sub> desorption (Figure 11d-f).<sup>143</sup>



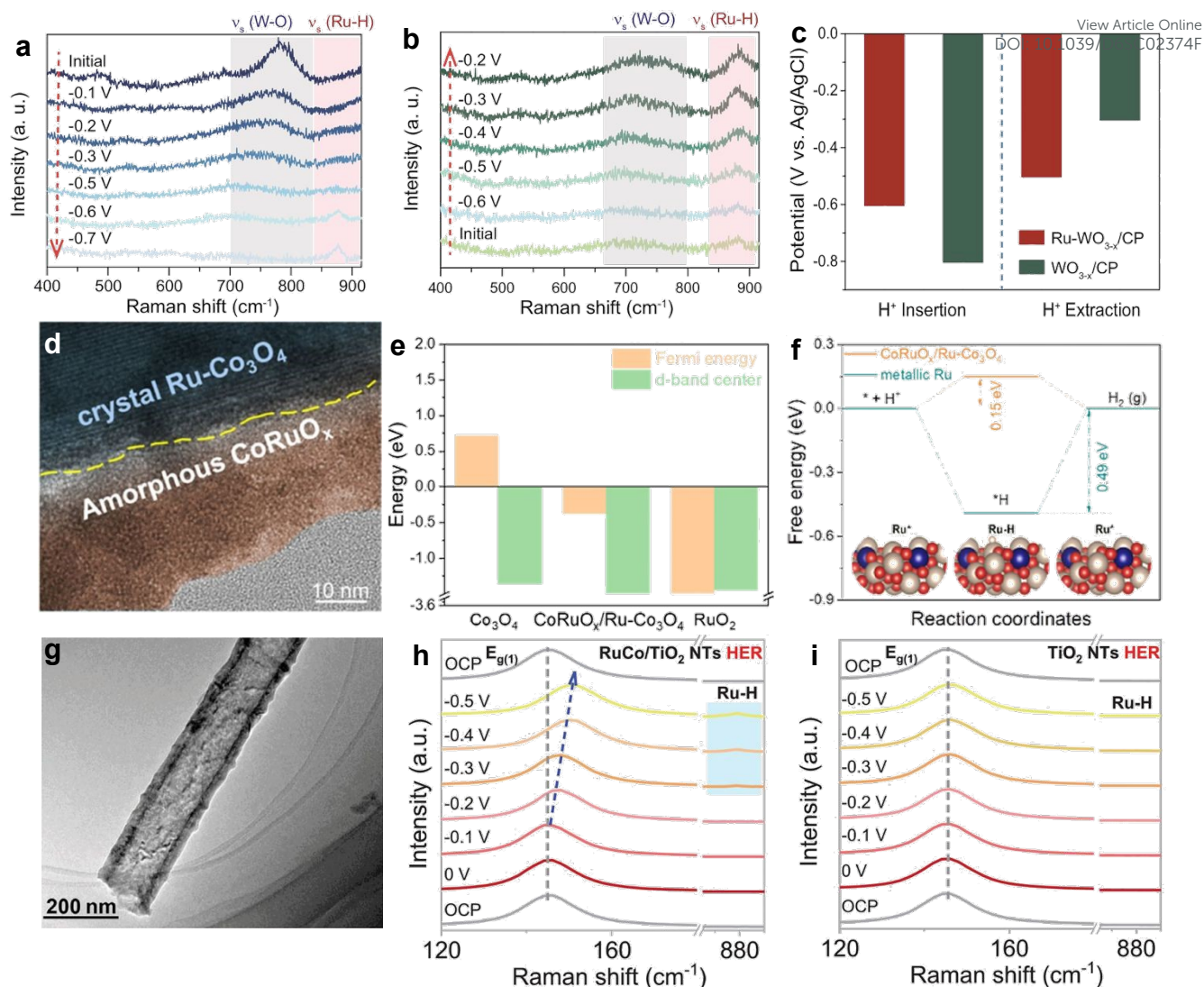


Figure 11 a) In situ Raman spectra acquired for Ru-WO<sub>3-x</sub>/CP across a potential range of -0.1 to -0.7 V vs. Ag/AgCl in 1.0 M PBS. b) In situ Raman spectra collected for Ru-WO<sub>3-x</sub>/CP in 1.0 M PBS over the potential range of -0.6 to -0.2 V vs. Ag/AgCl. c) Onset potentials for H<sup>+</sup> insertion and extraction in Ru-WO<sub>3-x</sub>/CP versus WO<sub>3-x</sub>/CP.<sup>136</sup> Copyright©2022, Springer Nature. d) TEM image of CoRuO<sub>x</sub>/Ru-Co<sub>3</sub>O<sub>4</sub>. e) The d-band center and Fermi energy of Co<sub>3</sub>O<sub>4</sub>, RuO<sub>2</sub> and CoRuO<sub>x</sub>/Ru-Co<sub>3</sub>O<sub>4</sub>. f) The free energy diagrams of the metallic Ru and CoRuO<sub>x</sub>/Ru-Co<sub>3</sub>O<sub>4</sub>.<sup>143</sup> Copyright©2025, Elsevier. g) TEM images of RuCo/TiO<sub>2</sub> NTs. in situ Raman spectra of h) RuCo/TiO<sub>2</sub> NTs and i) TiO<sub>2</sub> NTs from 0 to -0.5 V Ag/AgCl toward HER.<sup>147</sup> Copyright©2024, Wiley-VCH.

TiO<sub>2</sub>-based supports have emerged as an ideal platform for modulating the performance of Ru-based catalysts, owing to their excellent acidic stability, tunable surface chemistry, and abundant defect states. Among these, TiO<sub>2</sub> nanotube arrays, featuring large specific surface area and ordered structure, serve as ideal supports to promote the dispersion of Ru species and charge transport. Simultaneously, the Ti<sup>3+</sup> sites can establish enhanced metal-support interactions with Ru species, achieving functional complementarity through interfacial electron transfer, thereby synergistically optimizing the hydrogen evolution reaction pathway.<sup>144-146</sup> Following this design strategy, Chen et al. further introduced Co doping to prepare Co-doped Ru nanoparticles supported on TiO<sub>2</sub> nanotubes. They found that Co doping enhanced Ru-O-Ti bonding, thereby further strengthening the metal-support interaction. This strengthened interaction not only stabilized

the Ru species but also triggered the hydrogen spillover effect, significantly accelerating the hydrogen evolution kinetics (Figure 11g-i).<sup>147</sup>

Overall, the design strategies for 1D metal-based supports exhibit an evolutionary trend from single-component to multi-component hybrids and from static structures to dynamic interfaces. Unlike 0D supports, which rely primarily on specific surface area and interfacial density for modulation, the core advantage of 1D supports lies in their structural anisotropy, which enables directed charge/mass transport and long-range ordering. Metallic nanowires combine axial charge transport advantages with alloying and heterojunction construction to continuously optimize the electronic structure and reaction pathways of Ru, while oxide nanowires leverage oxygen vacancies and crystal phase engineering to achieve fine modulation of Ru while actively participating in catalysis. The



underlying logic is consistent: converting geometric anisotropy into dynamic control over the electronic states of Ru. This design space is uniquely accessible in 1D architectures. It is difficult to replicate in 0D systems. Looking forward, the key challenge lies in translating the long-range ordered features of 1D supports into designable synergistic catalytic interfaces and further exploring the potential of integrated arrays for optimizing macroscopic reaction mass transport. This not only builds upon the efforts to establish structure-performance relationships in 0D research but also extends into the design dimension of cross-scale synergy, opening new avenues for exploiting the unique advantages of 1D support systems.

### 3.3 2D metal-based supports

2D metal-based materials refer to sheet-like or layered structures with thicknesses in the nanometer scale (typically less than 10 nm), mainly including nanosheets, nanofilms, and nanonets. The extremely high specific surface area and in-plane anisotropy offer unique value for the design of ruthenium-based hydrogen evolution catalysts. The exposed planar atomic structure provides abundant active sites for reactant adsorption and activation, while the intact in-plane lattice continuity ensures efficient electron transport and accelerated interfacial charge transfer. Meanwhile, the layered structure allows facile modulation of the coordination environment and electronic states of surface atoms via doping, defect engineering, or surface modification.<sup>31</sup> Currently, 2D metal-based supports for hydrogen evolution catalysts mainly include Ru-based nanosheets, transition metal dichalcogenides, and MXene.

**3.3.1 Ru-based nanosheets.** Since the maturation of 2D metal synthesis techniques around 2018, substantial advances have been achieved in exploring ruthenium-based 2D nanomaterials as both active phases and supports. 2D Ru nanosheets combine the advantages of high specific surface area for active site exposure and ultrathin thickness for efficient charge transport, while Ru itself offers moderate hydrogen adsorption energy and excellent conductivity, making it an ideal candidate for the hydrogen evolution reaction.<sup>148</sup> However, pristine Ru nanosheets still face challenges such as suboptimal hydrogen adsorption energy, sluggish kinetics for water dissociation in alkaline media, and limited long-term durability. To tackle these obstacles, researchers have conducted systematic investigations from the perspectives of composition regulation, interface engineering, and defect design.

Early studies attempted to optimize the reaction pathway by introducing a second metal to construct bimetallic nanosheets. Ding et al. synthesized RuNi heteronanosheets with a phase-separated sandwich structure, where Ru selectively grew at both ends of the Ni columns to form intimate Ru-Ni interfaces. By constructing a large number of highly controllable heterointerfaces, they optimized the electronic structure and adsorption behaviour of intermediates (Figure 12a).<sup>149</sup> Liu et al. prepared RuNi alloys featuring a multilayer nanosheet architecture using a one-pot solvothermal approach. They

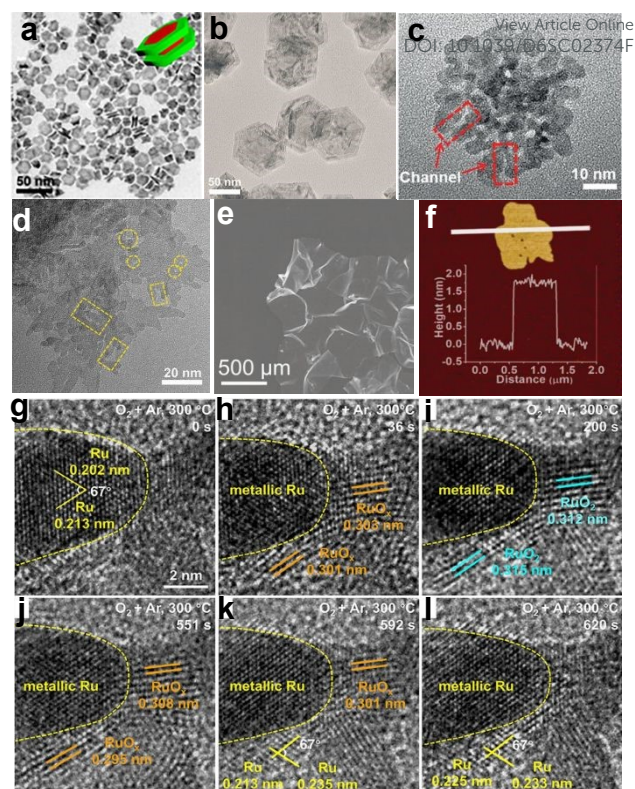


Figure 12 a) TEM image of Ru<sub>2</sub>Ni<sub>2</sub> SNs.<sup>149</sup> Copyright© 2018, Elsevier. b) Low-magnification TEM image of RuNi NSs.<sup>150</sup> Copyright© 2019, Elsevier. c) high-magnification TEM image of RuCu NSs.<sup>151</sup> Copyright© 2019, Wiley-VCH. d) TEM images of RuZn NSs.<sup>152</sup> Copyright© 2023, Wiley-VCH. e) FESEM and f) AFM and corresponding height profile of RuCo bimetallic nanosheets.<sup>153</sup> Copyright© 2023, Wiley-VCH. The reversible oxidation process of Ru nanosheets at 300°C under a 20% O<sub>2</sub>/Ar atmosphere. g–l) Time-resolved in situ TEM images of Ru nanosheets captured over 620 s. The area marked by yellow dashed lines maintains the metallic Ru, while peripheral areas undergo a reversible oxidation process.<sup>158</sup> Copyright© 2025, Wiley-VCH.

found that the introduction of Ni promoted water dissociation and optimized the hydrogen adsorption/desorption process, thereby synergistically accelerating the HER reaction kinetics (Figure 12b).<sup>150</sup> Yao et al. fabricated snowflake-like RuCu nanosheets with abundant channels. The unique structure combining crystalline Ru and amorphous Cu facilitated the accessibility of active sites while enhancing electrolyte infiltration and the release of gaseous products (Figure 12c).<sup>151</sup> As research progressed, alloying strategies were combined with phase engineering and heterostructure construction to achieve multidimensional optimization of catalytic performance.<sup>98</sup> Yu et al. synthesized ultrathin RuZn bimetallic nanosheets with a periodically stacked moiré superlattice structure. They found that electron donation from Zn to Ru caused a modest downward shift in the d-band center of surface Ru atoms, thereby expediting hydrogen desorption while also reducing the energy barrier for water dissociation (Figure 12d).<sup>152</sup> Jose et al. constructed atomically thin amorphous RuM (M = Co, etc.) bimetallics. They confirmed that Co played a promoting role in the reaction pathway by optimizing OH adsorption to facilitate water dissociation while simultaneously modulating the electronic structure of Ru (Figure 12e, f).<sup>153</sup>



Researchers have employed atomic-scale regulation strategies to systematically optimize 2D ruthenium-based nanosheets. These strategies include constructing in-plane superlattices, optimizing metal coordination numbers, introducing single-atom doping, or surface amorphization, which collectively enhance active site density, hydrogen intermediate adsorption behaviour, and reaction pathways.<sup>154,155</sup> Guided by theoretical predictions for experimental synthesis, Zhu et al. rationally constructed a layered Ru/RuS<sub>2</sub> heterostructure. They discovered that charge redistribution at the Ru/RuS<sub>2</sub> interface renders the surface Ru sites electron-deficient, optimizing the adsorption energies for both HER and OER intermediates.<sup>156</sup> Wang et al. doped Cu atoms into Ru/RuSe<sub>2</sub> heteronanosheets, where the synergistic effect between the heterointerface and Cu doping not only optimized the d-band center to inhibit overly strong proton binding but also lowered the reaction energy barrier by

enhancing H<sub>2</sub>O adsorption.<sup>157</sup> Using in-situ transmission electron microscopy, Xiao et al. observed a reversible phase transition from RuO<sub>2</sub> to Ru during the oxidation of Ru nanosheets, dominated by oxygen atom migration. This behaviour, which starkly contrasts with the unidirectional oxidation pathway of conventional metals, naturally generates abundant Ru-RuO<sub>2</sub> heterointerfaces, providing a large number of active sites for the alkaline HER (Figure 12g-l).<sup>158</sup>

**3.3.2 Transition metal dichalcogenides.** Layered transition metal dichalcogenides have become one of the earliest systematically studied 2D supports due to their electronically tunable properties and abundant edge-active sites. MoS<sub>2</sub>, as a representative example, possesses a layered structure in which covalently bonded S–Mo–S sheets are stacked via weak van der Waals interactions. Since researchers explicitly identified their edges as active centers for the hydrogen evolution reaction in 2008, this class of materials

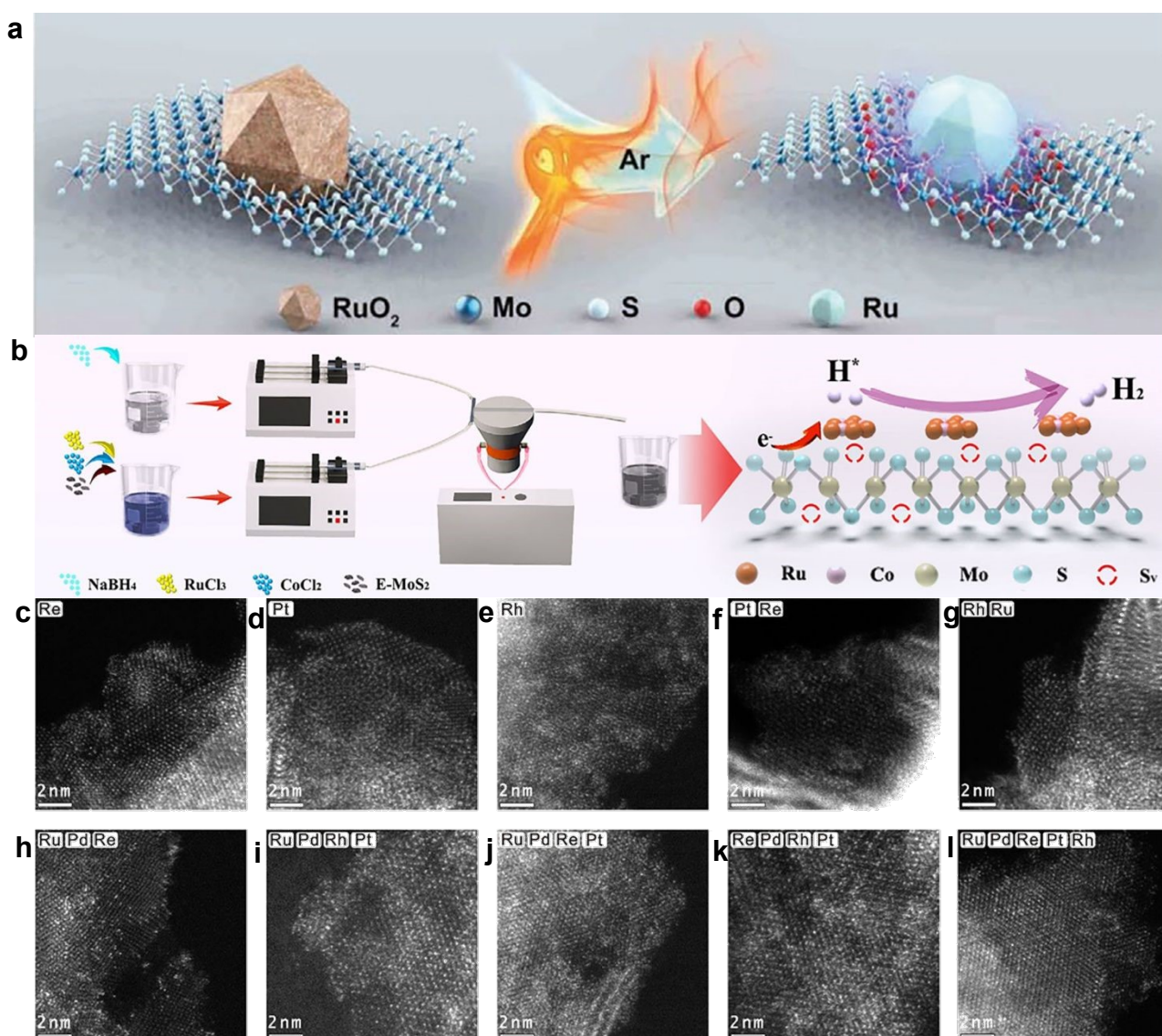


Figure 13 a) The fabrication process of MISC-1.<sup>163</sup> Copyright© 2021, Wiley-VCH. b) Schematic illustration of the synthetic process of the RuCo@E-MoS<sub>2,x</sub> NSs.<sup>164</sup> Copyright©2025, Wiley-VCH. c-l) Aberration-corrected HAADF-STEM images of high-loading monometallic SAs, multimetallic SAs and HESAs supported on TMDs. Scale bars, 2 nm.<sup>166</sup> Copyright© 2024, Wiley-VCH.



has been widely used as a platform for designing electrocatalysts.<sup>159</sup> However, a fundamental limitation has subsequently emerged: the basal plane of semiconducting transition metal dichalcogenides is catalytically inert, with active sites confined solely to the limited edge regions, severely restricting the overall catalytic efficiency.

The success of single-atom doping strategies has opened new avenues for unlocking the catalytic potential of the typically inert basal planes in transition metal dichalcogenides and has prompted researchers to explore more complex configurations of active centers.<sup>160,161</sup> Ge et al. extended the single-atom strategy to bimetallic systems by leveraging differences in electronegativity to co-modify MoS<sub>2</sub> with Ru and Ni dual single atoms. This study revealed that S atoms bonded to Ni acquire excess charge density to optimize H\* adsorption, while Ru atoms exhibit reduced charge density to facilitate OH<sup>-</sup> adsorption. This spatially synergistic division-of-labor mechanism effectively lowers the energy barrier of the Volmer step under alkaline conditions.<sup>162</sup> Building upon single-atom doping, strategies for constructing multi-active centers have been further expanded. Cai et al. employed a solid-phase interfacial reaction strategy, using RuO<sub>2</sub>/MoS<sub>2</sub> as a precursor to induce transformation at the interface, successfully introducing both oxygen vacancies and Ru metal centers into the MoO<sub>2</sub> plane. Theoretical calculations revealed that the adsorption free energies of both water and hydrogen intermediates in this Ru/MoO<sub>2</sub>-V<sub>O</sub> system are close to ideal values, confirming that the synergistic effect between oxygen vacancies and Ru sites not only substantially lowers the energy barrier for water dissociation but also optimizes the desorption step of hydrogen intermediates (Figure 13a).<sup>163</sup> Approaching from a synthetic methodology perspective, Su et al. utilized ultrasonic microreactor technology to achieve ultra-refined (~1.7 nm) and highly dispersed loading of RuCo alloys. They found that introducing Co modulates the electronic configuration of RuCo and creates robust interfacial coupling with the support. This synergistic effect lowers the Gibbs free energy for hydrogen adsorption on both Ru and Co sites while generating bimetallic active centers that circumvent the intrinsic competition between adsorption and desorption. (Figure 13b).<sup>164</sup>

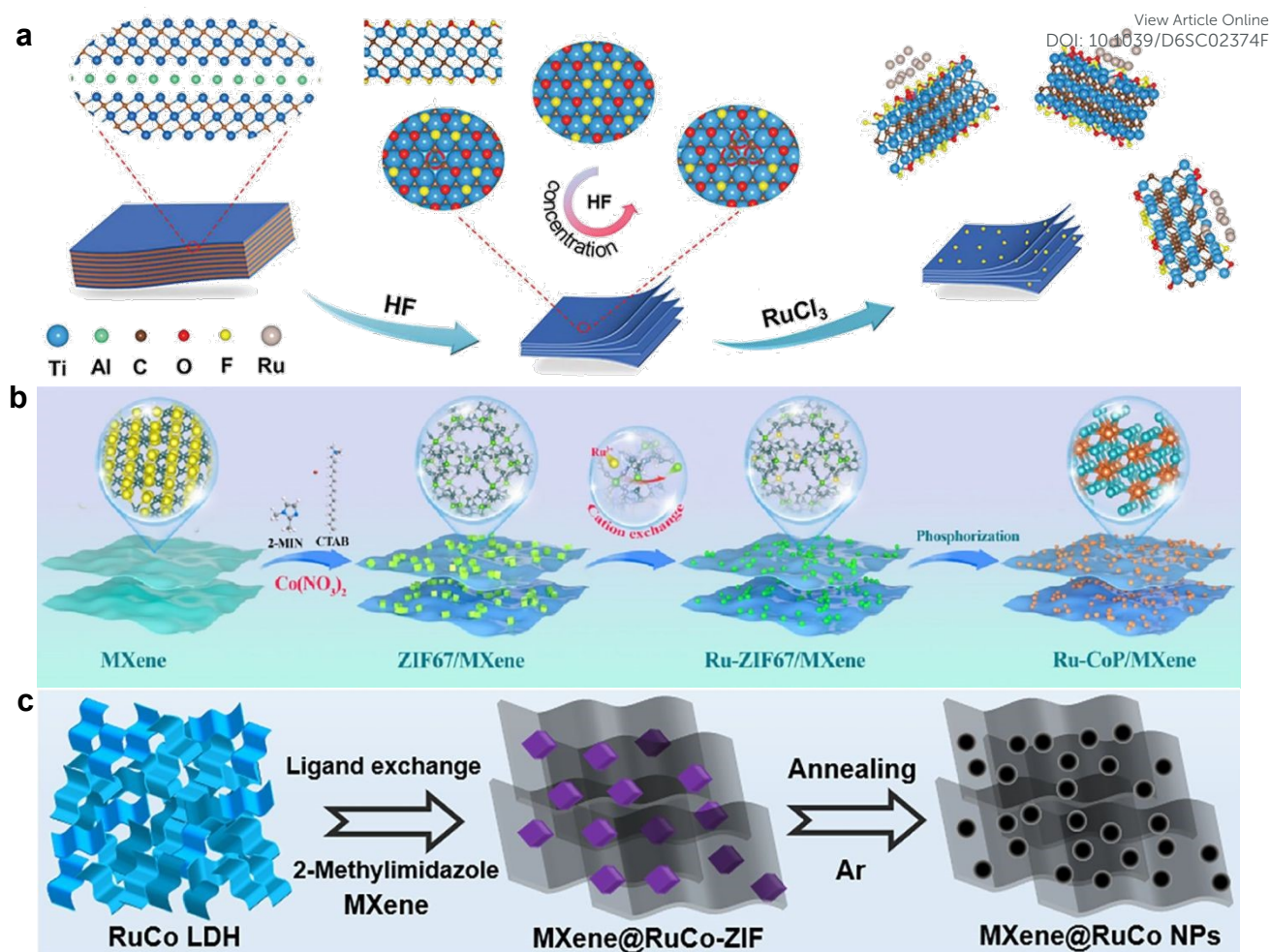
Researchers have also extended the single-atom strategy to other transition metal dichalcogenide systems, exploring higher-order forms of multi-metal synergy.<sup>165</sup> Luo et al. developed a substrate-mediated approach for constructing single-atom catalysts, successfully fabricating a series of multimetallic single-atom and high-entropy single-atom catalysts on MoS<sub>2</sub> and MoSe<sub>2</sub> supports. This strategy enables precise spatial positioning of the incorporated single atoms and allows for the continuous increase of metal content until the accessible Mo atoms on the support surface are fully substituted, thereby achieving higher metal loadings. In-depth studies revealed that this controlled synthesis is achieved by regulating the reversible redox reactions occurring at the interface between the transition metal dichalcogenides and

metal ions. This atomic-scale multi-metal synergistic regulation mechanism endows the high-entropy single-atom catalysts with activity and durability far exceeding those of commercial Pt benchmarks (Figure 13c-l).<sup>166</sup>

**3.3.3 MXene.** The emergence of MXene materials can be traced to 2011, when Gogotsi's team first successfully synthesized 2D Ti<sub>3</sub>C<sub>2</sub>T<sub>x</sub> through selective removal of the A layer from the MAX phase.<sup>167</sup> Over the following decade, hundreds of MXenes with diverse compositions and structures were synthesized, gradually forming a vast family of materials. These materials share the general formula M<sub>n+1</sub>X<sub>n</sub>T<sub>x</sub>, where M represents a transition metal (such as Ti, Nb, V, etc.), X is carbon or nitrogen, and T denotes surface terminal groups (e.g., -O, -OH, -F). By virtue of their unique layered structure, excellent metallic conductivity, hydrophilic surfaces, and highly tunable composition, MXenes exhibit distinct advantages in the field of electrocatalysis.<sup>33,168</sup> Notably, the rich surface chemistry of MXenes positioned them as ideal supports for single-atom catalyst design from the outset of their discovery. As early as 2019, Ramalingam et al. utilized Ti<sub>3</sub>C<sub>2</sub>T<sub>x</sub> MXene as a solid support to construct Ru single-atom active centers co-coordinated by nitrogen and sulfur on its surface, confirming that Ru single atoms coordinated with N and S sites on MXene were the origin of enhanced HER activity. This work inaugurated a series of subsequent explorations into modulating the electronic structure of active centers using MXene surface functional groups.<sup>21</sup> Following this line of inquiry, how to modulate the surface terminal groups of MXenes to optimize the catalytic activity of supported metals has emerged as a primary scientific question for this support system. Munkhjargal et al. modified the surface electronic structure of Ti<sub>3</sub>C<sub>2</sub>T<sub>x</sub> MXene through boron doping and found that B doping not only significantly improved the adsorption kinetics of H but also optimized the hydrogen adsorption free energy to a near-zero ideal value, while simultaneously reducing the charge transfer resistance, synergistically enhancing catalytic performance from both electron conduction and surface reaction perspectives.<sup>33</sup> Wang et al. prepared three types of MXene supports with different vacancy structures via controlled etching. Their study revealed that, unlike the terminal -O/-F coordination environment on conventional MXene surfaces, the titanium vacancy clusters within Ti<sub>3</sub>C<sub>2</sub>T<sub>x</sub>-V<sub>C</sub> establish a distinctive carbon-coordination environment from the lattice for Ru species, giving rise to exceptionally strong metal-support interactions. This interaction enables Ru clusters to achieve an optimal balance between the adsorption and dissociation of H<sub>2</sub>O as well as the desorption of OH and H species. (Figure 14a).<sup>169</sup>

Focusing on the rational design of active centers, researchers have further explored multi-component synergy and interface engineering strategies. Liu et al. incorporated Ru into CoP and then composited it with MXene, discovering that the incorporated Ru disrupts the rigid network structure of interfacial water, promotes water migration, and lowers the





water dissociation energy barrier. Simultaneously, the composite of Ru with MXene synergistically optimizes the d-band center of Co sites, thereby accelerating the Volmer step while balancing the adsorption/desorption behaviour of  $\text{H}^*$  (Figure 14b).<sup>170</sup> Li et al. derived Co-based nanoparticles from a MOF precursor and doped them with Ru, subsequently compositing the RuCo nanoparticles with MXene to construct a strongly interacting heterointerface. The doping of Ru introduces secondary active sites and reduces the nanoparticle size, substantially increasing the number of active sites. The MXene/RuCo NPs heterointerface generates a significant synergistic effect, lowering the work function of the catalyst and enhancing the charge transfer rate (Figure 14c).<sup>171</sup> Extending further to MAX phase materials, Wu et al. leveraged the excellent conductivity and abundant surface functional groups of 2D layered  $\text{Mo}_2\text{CT}_x$  MXene to anchor highly dispersed Ru clusters via an in-situ reduction strategy. They found that the interaction between Ru clusters modulates the electronic structure of the active sites, thereby promoting  $\text{H}_2\text{O}$  dissociation and hydrogen desorption.<sup>172</sup>

In summary, these studies demonstrate that the core advantage of 2D metal-based supports lies in the dual

accessibility afforded by their planar atomic structure: in-plane continuity provides efficient electron pathways, while out-of-plane exposure offers abundant active sites. This stands in stark contrast to the modulation mechanisms of zero-dimensional systems that rely on quantum size effects and one-dimensional architectures that leverage axial transport. It is this in-plane and out-of-plane synergy that enables 2D supports to serve simultaneously as both electronic modulators and active substrates. Ru-based nanosheets optimize intrinsic activity through alloying and defect design; transition metal dichalcogenides activate inert basal planes via single-atom doping; and MXene leverages its surface functional groups to achieve multi-center synergy. Looking forward, the central challenge lies in overcoming the intrinsic activity limitations of 2D supports: transforming inert in-plane regions into designable active interfaces and further exploring how layer stacking and hetero-integration can amplify synergistic catalytic effects. This not only builds upon the efforts to establish structure-performance relationships in zero-dimensional and one-dimensional research but also extends into the design dimension of in-plane and out-of-plane synergy, opening new



avenues for exploiting the unique advantages of 2D support systems.

### 3.4 3D metal-based supports

3D metal-based materials refer to porous or bulk structures not confined to the nanometer scale in spatial dimensions, whose continuous 3D network endows them with excellent structural stability and unique mass transport advantages. The interconnected porous channels accelerate reactant diffusion and gas release, while the high specific surface area provides abundant active sites and enables the confined anchoring of active components.<sup>35,173</sup> The 3D framework itself can serve as both a conductive substrate and structural support, eliminating the need for binders and enhancing the mechanical strength of the electrode. Furthermore, its open framework facilitates the optimization of the surface chemical environment through compositional regulation and functional modification.<sup>36</sup> Currently, 3D metal-based supports for hydrogen evolution catalysts mainly include aerogels, self-supporting electrodes, and metal-organic frameworks (MOFs).

**3.4.1 Aerogel.** Aerogel materials, by virtue of their ultra-high specific surface area, continuous three-dimensional porous network, and tunable electronic structure, provide an ideal platform for the dispersion and stabilization of Ru active centers. This unique structural feature not only ensures the high dispersion and effective anchoring of Ru species, but its open three-dimensional network also constructs fast mass transport pathways and fully exposed reaction interfaces. Researchers have constructed metal/oxide heterointerfaces through partial oxidation to tailor the binding strength of reaction intermediates, while additionally incorporating heteroatom

doping to prevent excessive oxidation of active components. This approach simultaneously boosts catalytic activity and durability while preserving the advantages of the three-dimensional structure.<sup>174</sup>

Building upon this foundation, researchers have delved into the influence mechanism of different types of heterophase interfaces on the hydrogen evolution reaction pathway by constructing various such interfaces. Fan et al. used Ru aerogels as a model system to investigate the interfacial interaction between Ru and CeO<sub>2</sub> by constructing CeO<sub>2</sub>-Ru aerogels featuring a heterogeneous Ru-O-Ce interface. The results revealed that electron redistribution at the heterogeneous Ru-O-Ce bridge enhances the interaction between Ru sites and hydrogen intermediates, while the CeO<sub>2</sub> sites exhibit faster water adsorption and dissociation capabilities. The 3D interconnected network of the aerogel not only provides abundant reaction sites for this interfacial synergy but also facilitates rapid transport of reactants and products through its open pores, thereby synergistically enhancing the hydrogen evolution kinetics (Figure 15a, b).<sup>175</sup> Liu et al. synthesized Cr<sub>0.033</sub>Ru<sub>0.967</sub> aerogels containing both face-centered cubic and hexagonal close-packed phases of Ru, discovering that the heterophase interface effectively weakens the excessively strong hydrogen adsorption at Ru sites. Furthermore, by incorporating Cr ions with high affinity for OH, they not only facilitated the desorption of OH from neighboring Ru sites but also modified the electronic environment surrounding Ru, which further lowered the binding energy of OH on Ru. This work demonstrates that combining crystal phase engineering with heteroatom doping enables the synergistic modulation of multiple reaction intermediates within 3D aerogels.<sup>176</sup>

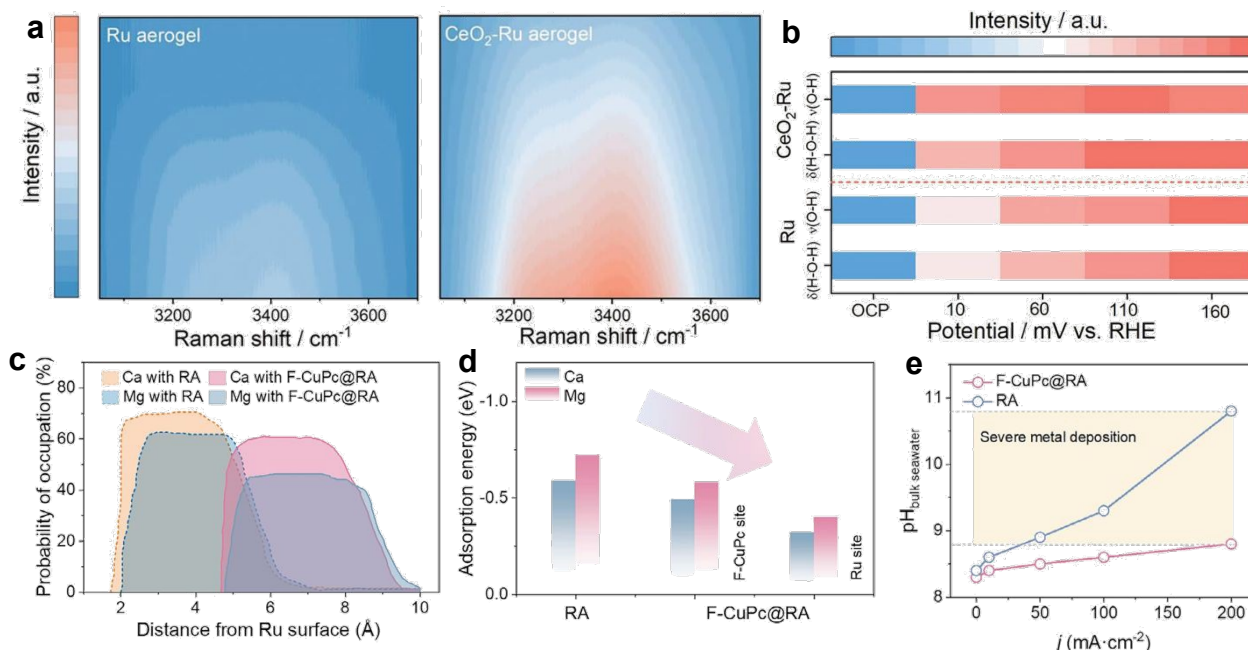


Figure 15 a) The isotherm diagrams of  $\nu(\text{O-H})$  signal for Ru and CeO<sub>2</sub>-Ru aerogel. b) Corresponding intensity differences of HER intermediates.<sup>175</sup> Copyright©2025, Wiley-VCH. c) Distribution characteristics of Ca and Mg cations on the catalyst surface. d) Adsorption energy of catalysts for Ca and Mg cations. e) pH of the bulk seawater near the cathode in the process of electrolysis of natural seawater.<sup>177</sup> Copyright©2025, Wiley-VCH.



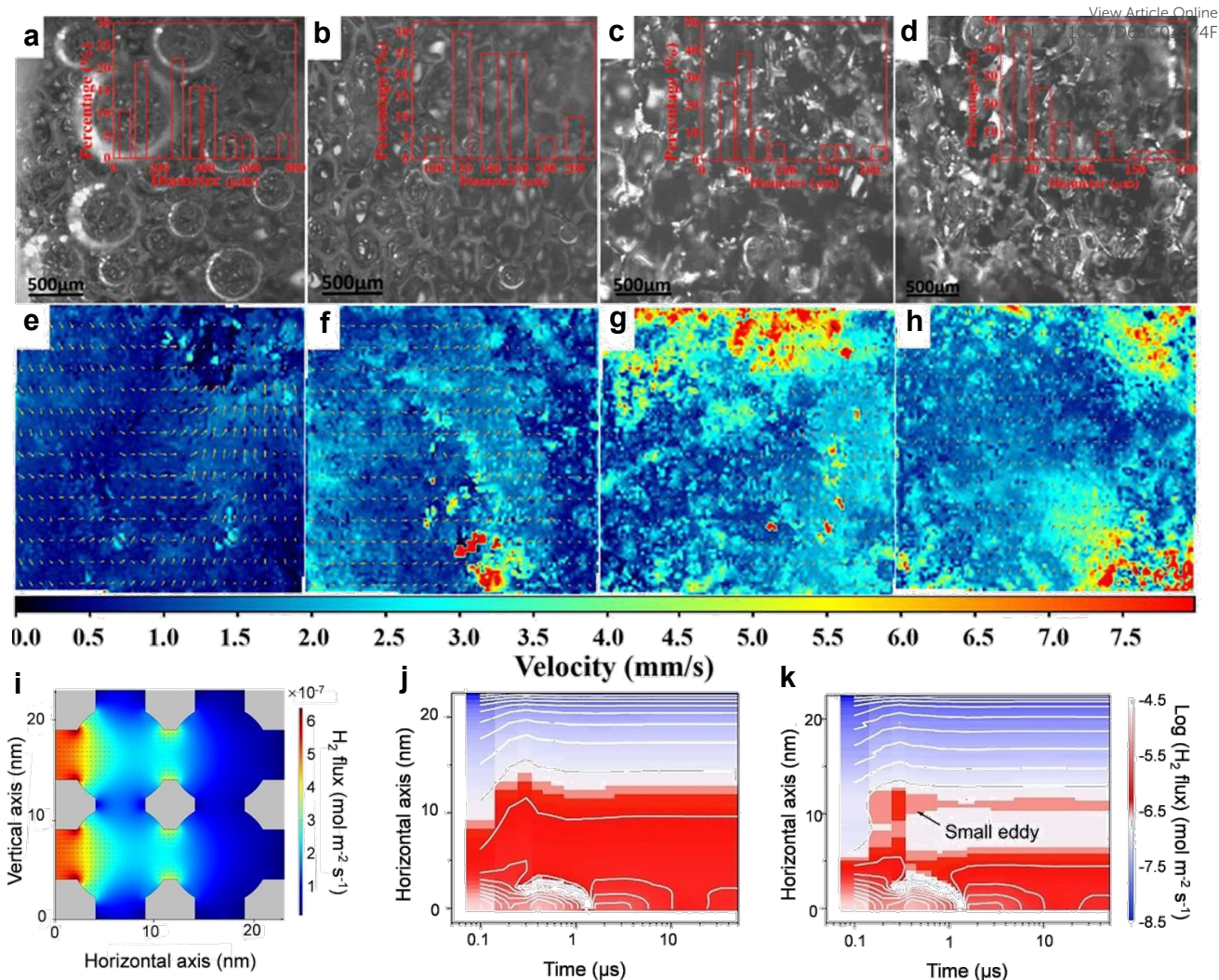


Figure 16 Digital images capturing bubble evolution behaviour on a) NF, b) Ru/NF, c) c-Ti<sub>3</sub>C<sub>2</sub>T<sub>x</sub>/NF, and d) Ru/c-Ti<sub>3</sub>C<sub>2</sub>T<sub>x</sub>/NF electrodes at a current density of 20 mA cm<sup>-2</sup>. The associated fluid velocity vector fields near the electrode surfaces for e) NF, f) Ru/NF, g) c-Ti<sub>3</sub>C<sub>2</sub>T<sub>x</sub>/NF, and h) Ru/c-Ti<sub>3</sub>C<sub>2</sub>T<sub>x</sub>/NF.<sup>184</sup> Copyright©2021, Elsevier. i) H<sub>2</sub> flux distribution within the mesopore channels of Ru/3D-OMC models. Two-dimensional contour plots depicting log(H<sub>2</sub> flux) as a function of time and position along the x-axis for j) Ru/2d-OMC and k) Ru/3d-OMC models with a fixed y-axis position of 16.3 nm.<sup>16</sup> Copyright© 2023, Wiley-VCH.

In addition, Chen et al. combined the structural advantages of aerogels with surface functionalization design to create an intelligent phthalocyanine-armed ruthenium aerogel electrocatalyst. This addresses the issue of insoluble deposits (such as Mg and Ca hydroxides/carbonates) forming on the cathode in complex seawater environments, which block active sites, leading to catalyst deactivation and electrolysis failure. This design utilizes the armor layer to promote water splitting and self-trap protons, constructing a localized acidic environment on the electrode surface and forming a positively charged protective layer that effectively shields against the approach and deposition of cations such as Mg<sup>2+</sup> and Ca<sup>2+</sup> from seawater. Simultaneously, the unsaturated Lewis acid sites at the phthalocyanine centers can bind OH<sup>-</sup>, mitigating the rise in interfacial pH and fundamentally preventing precipitate formation (Figure 15c-e).<sup>177</sup>

**3.4.2 Self-supporting electrode.** The development of 3D self-supporting electrodes originated from a rethinking of the issues

inherent in traditional coated electrodes, such as the easy burial of active sites, high interfacial resistance, and insufficient stability. At the beginning of this century, researchers began to directly grow active components on three-dimensional conductive substrates to enhance mass transfer efficiency and structural stability. Around 2010, with advancements in nanofabrication techniques, various transition metal compounds were successfully grown in situ on substrates such as nickel foam and carbon cloth, and their advantages were systematically revealed: the continuous conductive network ensures rapid electron transport, while the open hierarchical pores facilitate electrolyte penetration and gas release.<sup>178,179</sup> In recent years, the research focus has expanded from morphological control to the synergistic optimization of electronic structure and mass transport properties, leading to the development of general design strategies centered on the electronic regulation of active sites and the enhancement of mass transfer through hierarchical pores.



Leveraging the structural advantages of 3D self-supporting electrodes, researchers have further optimized their hydrogen evolution performance through various atomic-scale modulation strategies. For instance, constructing Ru-doped heterostructures enables collective modulation of the electronic states of multi-metal sites, optimizing water adsorption/desorption and proton adsorption behavior;<sup>180</sup> introducing defects and establishing metal-oxygen bridging structures can modulate the d-band center and interfacial charge transfer, enhancing structural stability.<sup>181</sup> Furthermore, constructing a robust metal-support interface can promote the ordered alignment of water molecules at the interface and reinforce the network of hydrogen bonds to facilitate mass transport;<sup>182</sup> while single-atom doping strategies can fine-tune how reaction intermediates bind to the surface via charge redistribution across the interface.<sup>183</sup> These studies collectively demonstrate that 3D self-supporting electrodes, as a structural platform, offer broad scope for multi-dimensional design ranging from electronic state modulation to interfacial microenvironment optimization.

Addressing the core design dimension of enhancing mass transfer and bubble detachment, researchers have primarily focused on regulating electrode surface characteristics, constructing pore structures, and achieving integrated assembly of active components with the substrate, aiming to ensure effective exposure of active sites and timely supply of reactants at high current densities. Modulating the surface wettability and bubble adhesion behaviour of the electrode is a direct approach to optimizing the gas-liquid-solid three-phase interface. Kong et al. fabricated a Ru/MXene three-dimensional electrode on porous nickel foam utilizing  $\text{Ti}_3\text{C}_2\text{T}_x$  nanosheets as a structural mediator, endowing it with both superaerophobic and superhydrophilic properties. The synergistic interplay between Ru and  $\text{Ti}_3\text{C}_2\text{T}_x$  enhanced the kinetics of water dissociation and the subsequent evolution of  $\text{H}_2$ . The study revealed that the diameter of hydrogen bubbles on the  $\text{c-Ti}_3\text{C}_2\text{T}_x/\text{NF}$  loaded with Ru was significantly reduced. This rapid detachment of small bubbles effectively prevented the deactivation of active sites caused by bubble coverage under high current densities (Figure 16a-h).<sup>184</sup> Wu et al. also pointed out that for amorphous  $\text{RuO}_2$ -decorated  $\text{FeOOH}$  nanosheets synthesized on iron foam via a one-pot corrosion strategy, the synergistic effect of superhydrophilicity and superaerophobicity was likewise a key factor in enhancing hydrogen evolution performance. Contact angle measurements showed that the electrode exhibited superhydrophilic characteristics, along with an increased bubble contact angle indicating excellent superaerophobicity, which promoted rapid detachment of generated bubbles and prevented active sites from being occupied by bubbles, thereby maintaining continuous contact between the active interface and the electrolyte.<sup>185</sup>

In addition to surface property regulation, rational design of the electrode's pore structure is equally crucial for improving mass transfer efficiency. Liu et al. pointed out the inherent

shortcomings of conventional catalyst structures in efficiently releasing bubbles and introduced a nanoscale-grade separation strategy based on ordered three-dimensional networks of sub-5 nm mesopores to address this issue. Their study found that this criss-crossing mesoporous architecture with spatial separation facilitated the efficient transport of  $\text{H}_2$  bubbles through the interconnected pore channels. (Figure 16i-k).<sup>16</sup>

**3.4.3 Metal organic framework.** MOFs constitute a class of periodic porous materials derived from the coordination-driven assembly of inorganic metal nodes with organic ligands. Due to their high specific surface area, well-defined crystalline structure, and tunable pore sizes, they exhibit significant advantages in the field of electrocatalysis. The ordered pores of MOFs can confine and stabilize Ru active species, preventing their agglomeration, while their abundant functional groups act as proton mediators to synergistically modulate the reaction microenvironment.<sup>186</sup> Although MOFs intrinsically possess poor electrical conductivity, these limitations are being progressively overcome through strategies such as elemental doping, heterostructure construction, and the derivation of carbon materials. This positions MOFs as an important platform for 3D material design, offering new strategies for enhancing the efficiency of the hydrogen evolution reaction.

Research on introducing Ru species into Ni-based MOFs has demonstrated that constructing well-defined Ni-O-Ru interfacial bonds can trigger electron redistribution, optimize the adsorption free energy of water and hydrogen intermediates, and achieve efficient hydrogen evolution over a wide pH range.<sup>187</sup> Li et al. further developed a  $\text{NiFeRu}_{\text{SA+NP}}\text{-DOBDC}$  material featuring the coexistence of Ru single atoms and Ru nanoparticles. By simultaneously regulating the distribution of these two Ru species, they achieved synergistic optimization of the hydrogen evolution reaction pathway. In-situ analysis and theoretical calculations jointly confirmed that the Ru single atoms and Ru nanoparticles collectively accelerate the Volmer-Heyrovsky pathway, significantly enhancing the hydrogen evolution kinetics (Figure 17a-c).<sup>188</sup> To address the issue of insufficient driving force for hydrogen spillover in single-component catalysts, Zhang et al. constructed an amino-functionalized NiRu-MOF. They utilized the frustrated Lewis pairs (Ni-NH<sub>2</sub>) spontaneously formed within the framework as synergistic active centers to establish continuous short-range hydrogen spillover pathways. The Ni-NH<sub>2</sub> sites efficiently adsorb and dissociate water molecules and promote proton transport, while the adjacent Ru sites benefit from the electronic modulation by the amino groups, which lowers the energy barrier for hydrogen desorption. The significant impairment of catalytic activity upon blocking the FLPs confirms their central role.<sup>189</sup>

Beyond Ni-based MOFs, researchers have also extended the metal nodes of MOF supports to other systems such as Co and Fe. Through heteroatom doping or interfacial bonding engineering, they have achieved electronic structure modulation of Ru active centers and multi-component



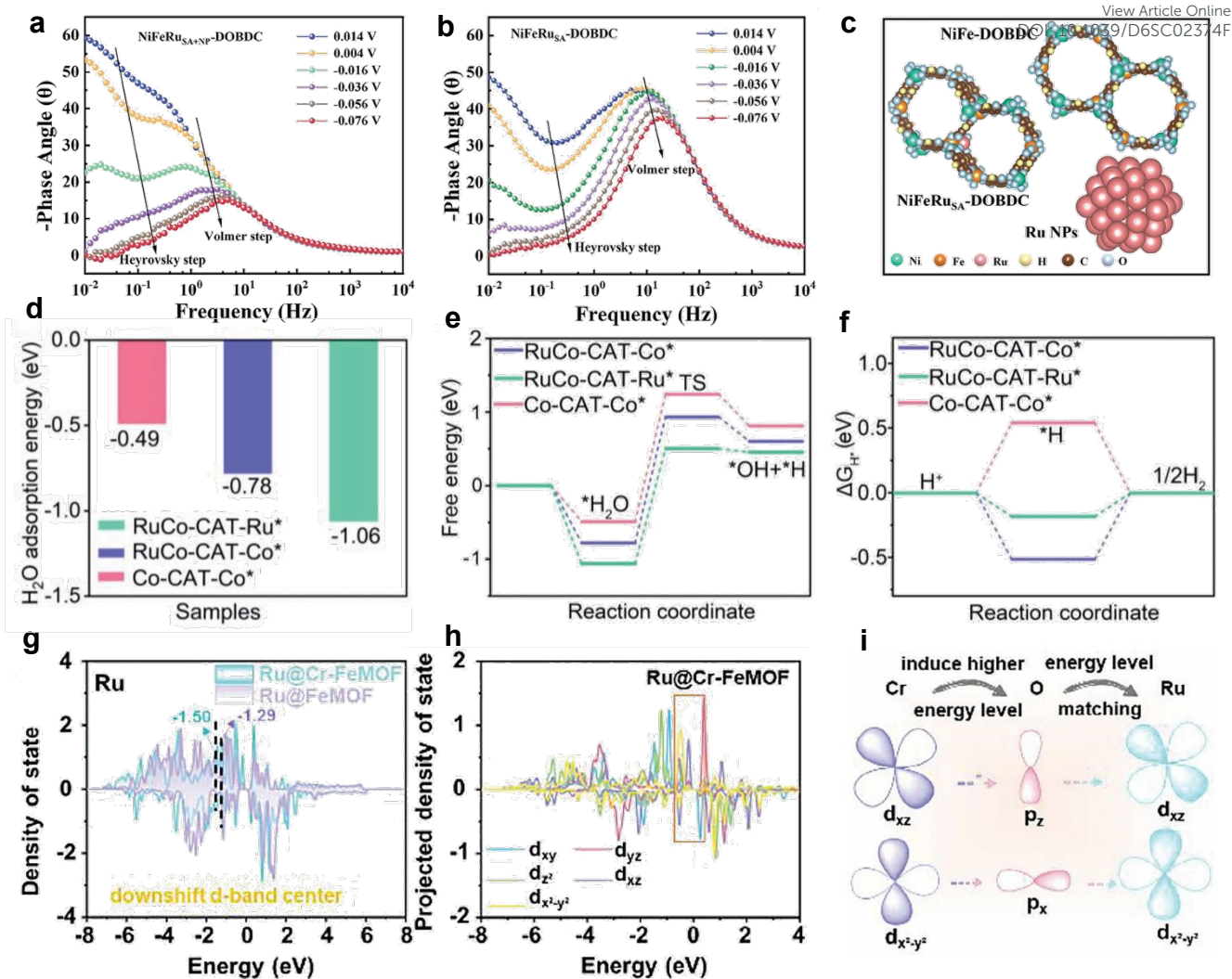


Figure 17 In situ EIS tests of a) NiFeRu<sub>SA+NP</sub>-DOBDC and b) NiFeRu<sub>SA</sub>-DOBDC under applied potentials in 1 M KOH solution. c) Optimized structure models of NiFe-DOBDC, RuNPs, and NiFeRu<sub>SA</sub>-DOBDC.<sup>188</sup> Copyright©2024, Wiley-VCH. d) Adsorption energy of H<sub>2</sub>O, e) Energy diagram for H<sub>2</sub>O dissociation, f) Free energy diagram for hydrogen adsorption at Ru and Co sites in RuCo-CAT, alongside Co sites in Co-CAT.<sup>190</sup> Copyright©2023, Wiley-VCH. g) Calculated density of states for Ru active sites in Ru@Cr-FeMOF and Ru@FeMOF. PDOS curves of Ru d orbitals of h) Ru@Cr-FeMOF. i) Schematic illustration depicting the orbital modulation of ruthenium nanoclusters by the Cr–O–Ru interface.<sup>191</sup> Copyright©2023, Wiley-VCH.

synergistic optimization. In the Co-based MOF system, He et al. successfully constructed a dual-active-site catalytic system by doping Ru atoms into a Co-catecholate MOF. Theoretical calculations revealed that the doped Ru sites possess optimal hydrogen intermediate adsorption free energy, significantly outperforming the Co sites within the MOF. Concurrently, the introduction of Ru enhanced the conductivity and water adsorption capacity of the MOF framework, lowering the energy barrier for water dissociation (Figure 17d-f).<sup>190</sup> Regarding heterometal doping strategies, Zhao et al. anchored ultra-low loading Ru nanoclusters onto a Cr-doped Fe-MOF support, achieving stable integration of Ru species with the MOF framework through robust Cr–O–Ru chemical bonds. This interfacial bonding strategy effectively modulated the electronic structure of Ru sites: on one hand, it upshifted the highest occupied d-orbital of Ru sites closer to the Fermi level, facilitating charge transfer with oxygen intermediates during the oxygen evolution reaction; on the other hand, it

downshifted the d-band center of Ru, weakening the excessive adsorption of hydrogen atoms, thereby simultaneously optimizing the hydrogen evolution reaction pathway (Figure 17g-i).<sup>191</sup>

The typical differences in spatial scale, electronic regulation scope, and charge transfer amount to Ru for supports of different dimensions are summarized in Table 1. In summary, reflecting on the progression from 0D to 3D supports, a fundamental question emerges: what is it that we truly seek from a support? 0D systems revealed the richness of interfacial chemistry; 1D architectures demonstrated the importance of directional transport; 2D materials established the power of in-plane synergy. Upon reaching 3D, however, the answer appears to shift from "more" or "stronger" toward "integration." Rather than pursuing optimization along a single dimension, 3D supports integrate electron conduction, mass transport, active site dispersion, and interfacial microenvironment modulation into a continuous network. This suggests that the goal of



support design may not be an optimal solution in any individual dimension, but rather a balanced trade-off under multi-dimensional constraints. Future efforts may therefore focus less on developing increasingly complex structures and more on understanding how designs across different scales operate in concert—specifically, how electronic modulation at the atomic level interfaces with mass transport networks at the micron scale. This is

a question that low-dimensional supports struggle to address—one that 3D architectures are only beginning to answer. A comprehensive comparison of the advantages, limitations, and suitable application scenarios for each category of catalyst dimensions is summarized in Table 2.

Table 1 Typical differences in MSI characteristics for Ru-based catalysts supported on different dimensional structures.

Dimension	Spatial Scale of MSI	Scope of Electronic Regulation	Typical Charge Transfer to Ru
0D	Localized at the discrete particle–particle or particle–support interface	Limited to individual Ru nanoparticles or single atoms; weak long-range effect	Low to moderate
1D	Extended along the axial direction of the 1D support	Regulated along the electron transport pathway; enhanced local electric field at tips	Moderate
2D	Distributed across the basal plane and edges of the 2D support	Regulated over the entire 2D plane; strong coupling with abundant edge sites	Moderate to high
3D	Macroscopic 3D network; interface effects extend throughout the porous structure	Holistic regulation across the entire 3D skeleton; synergistic effect from hierarchical porosity	High

Table 2 Dimensional engineering of Ru-based HER catalysts: a comparative summary.

Dimension	Carrier type	Advantage	Limitation	Typical Applications
0D	Nanoparticles	High surface area; good dispersion; quantum effects	Agglomeration; poor stability under harsh conditions	Seawater electrolysis; surface engineering
0D	Nanoclusters	Strong cluster-support coupling; hydrogen spillover	Easy agglomeration; complex active site identification	Alkaline HER; spillover-mediated catalysis
0D	Nanocrystals	Ordered lattice; abundant defects; tunable phases	Complex synthesis; phase stability concerns	Mechanistic studies; phase-dependent catalysis
1D	Metallic nanowires	Fast axial charge transport; high flexibility	Lower surface area than 0D/2D	PEMWE; flexible electrodes
1D	Metallic oxides nanowires.	Strong MSI; oxygen vacancies; good acidic stability	Lower conductivity; potential phase transformation	Acidic HER; spillover-mediated catalysis
2D	Ru-based nanosheets	High surface area; efficient charge transport	Nanosheet restacking; limited long-term stability	High-performance alkaline HER
2D	Transition metal dichalcogenides	Abundant edge sites; tunable electronic structure	Inert basal plane; requires defect engineering	Single-atom/dual-atom catalysts; pH-universal HER
2D	MXene.	High conductivity; hydrophilic surface; ideal single-atom support	Surface oxidation; complex synthesis	Strongly coupled interfaces; single-atom catalysts
3D	Aerogel	Ultra-high surface area; continuous porous network; fast mass transport	Complex synthesis; mechanical fragility; high cost	Industrial high-current-density operation
3D	Self-supporting electrode	Binder-free; excellent stability; rapid bubble detachment	Substrate-dependent; limited substrate geometries	Practical AEMWE/PEMWE; industrial-scale production
3D	Metal organic framework	High surface area; tunable pores; precise active site engineering	Low conductivity; poor hydrolytic stability	Dual-active-site catalysis; well-defined coordination environments

## 4 Operando Dynamic Evolution of Ru-Based Catalysts for the HER

Understanding the true active sites of electrocatalysts under working conditions is key to rationally designing high-performance catalysts. In situ and operando studies on Ru-based HER catalysts have revealed that their surface structure and valence state are not static, but undergo significant dynamic changes with applied potential. In alkaline HER, operando characterization consistently shows that the valence state of Ru exhibits complex dynamic behavior under reductive potentials, with the direction of evolution strongly depending on the initial catalyst structure. Zhao et al. used in situ XPS to track the valence changes of Ru in the Ru@NMoC catalyst during alkaline HER. They found that upon applying a cathodic potential, the Ru 3p peak shifted to a lower binding energy,

indicating the reduction of Ru<sup>3+</sup> or Ru<sup>4+</sup> species to more active low- or zero-valent metallic Ru. This observation was further supported by in situ XANES, where the Ru absorption edge shifted to lower energy as the potential became more negative (Figure 18a, b).<sup>192</sup> In contrast, Zhao et al. observed an opposite trend in a Ru/WO<sub>x</sub> system. In situ XPS revealed that metallic Ru<sup>0</sup> was gradually oxidized to Ru<sup>3+</sup> or Ru<sup>4+</sup> during HER, and interestingly, the content of this partially oxidized Ru species showed a positive linear correlation with HER activity. This suggests that a moderately oxidized Ru surface may be more favorable for water dissociation than a fully metallic Ru surface in alkaline media (Figure 18c).<sup>140</sup> Additionally, Sun et al. discovered a reversible valence change in the Ru<sub>SA</sub>-CoP system. The valence of Ru increased from +3 (before the reaction) to +4 (during the reaction), then returned to +3 after the voltage was removed. This reversible change demonstrates that the



coordination structure of Ru undergoes dynamic self-adaptation under operating conditions (Figure 18d).<sup>125</sup>

In acidic media, conventional RuO<sub>2</sub> is prone to over-oxidation, forming soluble RuO<sub>4</sub> and leading to the loss of active species. However, through sophisticated interface engineering and coordination design, the stability and activity of Ru under acidic conditions can be significantly improved. Fan et al. used in situ XAS and in situ XRD to reveal a two-step reconstruction process of the double perovskite Ca<sub>2</sub>CoRuO<sub>6</sub> during acidic HER. At the initial stage, Ru<sup>5+</sup> was rapidly reduced to Ru<sup>3+</sup>, while the perovskite structure remained intact. After 2 h of reaction, Ru was further reduced to its metallic state and self-assembled into a Co-doped Ru metal cluster layer on the support surface, eventually forming a Co–Ru/CCRO composite structure. This work clearly demonstrates that the true catalyst is no longer the initial CCRO perovskite, but the in situ formed Co–Ru/CCRO (Figure 18e–g).<sup>193</sup> In another study, Wang et al. designed a Pt

single-atom catalyst synergistically stabilized by Cl ligands and a Ru support. They used in situ XAS and operando Raman spectroscopy to monitor the evolution of the Pt and Ru coordination environments under acidic conditions in real time. Under reductive potentials, the initial RuO<sub>x</sub> surface layer was partially reduced to metallic Ru. Meanwhile, Pt–O coordination gradually disappeared, while Pt–Ru and Pt–Cl coordinations emerged successively, forming a dynamically stable Pt–Cl–Pt bridging structure. In contrast, a Cl-free control sample showed an increase in Pt–Pt coordination under the same conditions, indicating severe aggregation.<sup>95</sup> This work provides direct spectroscopic evidence for stabilizing noble metal single atoms under harsh acidic conditions through coordination engineering.

In summary, the in situ and operando findings described above suggest that the initial structure of Ru based catalysts is often just a precursor or a precatalyst. Under real working conditions, that is, under an applied reductive potential in an

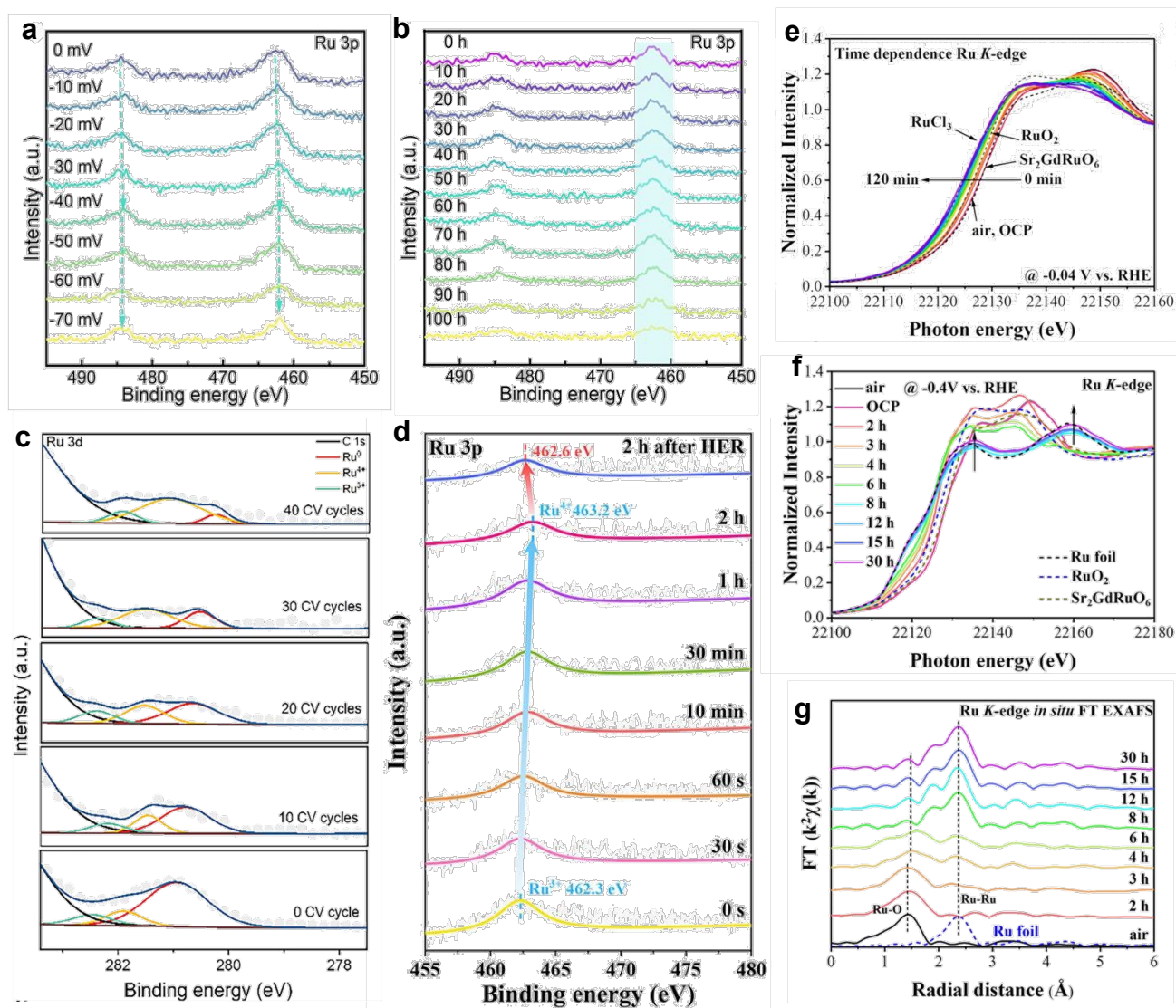


Figure 18 a) In-situ XPS spectra of Ru 3p at different potentials. b) XPS spectra of Ru 3p measured every 10 h at a current density of 100 mA cm<sup>-2</sup>.<sup>192</sup> Copyright© 2025, Wiley-VCH. c) Ru 3d XPS spectra for RWO recorded with increased CV cycles from 0.15 to -0.75V versus RHE.<sup>140</sup> Copyright©2025, Wiley-VCH. d) The Ru 3p peak of Ru<sub>5d</sub>-CoP during the whole HER process in 1.0 m KOH.<sup>125</sup> Copyright©2025, Wiley-VCH. e) Time-dependent XANES spectra at the Ru K-edge of the CCRO sample and relative references. f, g) in situ XANES and EXAFS at the Ru K-edge of CCRO and references.<sup>193</sup> Copyright©2025, The Royal Society of Chemistry.



electrolyte environment and during hydrogen adsorption, their surfaces undergo significant changes in valence state and coordination structure. In alkaline media, the valence state of Ru can either decrease to metallic Ru or increase to a partially oxidized state denoted as Ru<sup>n+</sup>. The former favors hydrogen adsorption, while the latter promotes water dissociation. In acidic media, perovskite type Ru based catalysts can reconstruct into metal cluster on support structures, whereas single atom Ru based catalysts can form stable ligand bridged structures to prevent aggregation. Therefore, combining multiple in situ and operando spectroscopic techniques, especially X ray absorption spectroscopy, X ray photoelectron spectroscopy, and Raman spectroscopy, for real time monitoring plays an irreplaceable role in accurately identifying active sites and guiding catalyst design.

## 5 Device-Level Applications of Ru-Based Catalysts

When moving from half-cell tests to practical AEMWE or PEMWE devices, electrocatalysts often show a significant performance gap. This gap becomes especially pronounced under industrial operating conditions with high current densities ( $\geq 1$  A cm<sup>-2</sup>). It mainly arises from differences in mass transport, ohmic losses, catalyst utilization, and long-term stability.<sup>194,195</sup> Due to their inherent physicochemical characteristics, catalyst structures with different dimensions each have their own advantages and limitations in industrial applications.

0D nanoparticles are the most widely studied catalyst morphology. Their advantages include simple synthesis, controllable particle size, and good batch-to-batch consistency. For example, Mn-RuO<sub>2</sub> nanoparticles achieve an industrial current density of 1.0 A cm<sup>-2</sup> at just 1.87 V in a two-electrode alkaline flow cell.<sup>103</sup> Ru-WC<sub>1-x</sub> composites deliver stable performance in an AEMWE at 70°C, reaching 0.5 A cm<sup>-2</sup> at a cell voltage of 1.73 V.<sup>196</sup> However, the challenges of 0D catalysts at the device level stem from their discrete nature. They typically require binders such as Nafion to attach to the electrode, which can block active sites and introduce inter-particle contact resistance. More importantly, under high current densities, intense bubble evolution can easily detach catalyst particles from the substrate, becoming a major cause of performance decay.<sup>197</sup> It is worth noting that with optimized electrode fabrication methods and strong metal-support interactions, some 0D catalysts have achieved stable operation for 1000 h in a PEMWE.<sup>95</sup> This demonstrates that 0D structures still hold irreplaceable value in large-scale production and cost-sensitive applications.

1D nanowires or nanoneedle arrays fall somewhere in between. Their axial electron transport pathways and tip-enhanced local electric field effects give them better charge transfer kinetics than 0D catalysts. Li<sub>3.0</sub>RuSn<sub>0.8</sub> nanowires operate stably for 1000 hours in an AEMWE at 1.0 A cm<sup>-2</sup> with a cell voltage of 1.689 V. Their mass activity reaches 10.89 A

mg<sub>Ru</sub><sup>-1</sup>, which is 4.11 times higher than that of commercial Pt/C.<sup>128</sup> However, the limitations of 1D structures also come from their geometry. The narrow gaps between nanowires can create mass transport bottlenecks at high current densities. Meanwhile, the tip structures face risks of dissolution and erosion during long-term electrochemical operation.<sup>198</sup> Therefore, 1D structures are more competitive in applications that require fast response and operate at moderate current densities.

2D nanosheets are ideal platforms for supporting single atoms or constructing heterointerfaces, thanks to their high specific surface area and abundant edge sites. L-Ru/Co(OH)<sub>x</sub> and Ru-Ni<sub>3</sub>N nanosheets deliver excellent performance in AEMWEs, achieving 1.68 A cm<sup>-2</sup> at 2.0 V and 1.0 A cm<sup>-2</sup> at 1.79 V, respectively, while maintaining stability for hundreds of hours.<sup>182,199</sup> However, 2D materials have an inherent limitation: a strong tendency to stack. The van der Waals forces between layers, which arise from their high surface area, cause nanosheets to inevitably stack during electrode fabrication and operation. This stacking blocks mass transport channels, hinders electrolyte penetration, and impedes gas release. This limitation becomes especially severe at high current densities, making it a difficult performance bottleneck for 2D structures to overcome.<sup>200</sup> Despite this, 2D materials still offer unique advantages in flexible electrode design and lightweight applications.<sup>201</sup>

3D self-supported porous structures exhibit the best overall performance at the device level. This class of materials includes aerogels and porous frameworks grown in situ on metal foams. By integrating the catalyst directly onto a conductive substrate, these structures fundamentally avoid the detachment issues of 0D particles and the stacking problems of 2D sheets. Their open and interconnected pore networks provide smooth and unblocked pathways for electrolyte infiltration and gas release. The CeO<sub>2</sub>-Ru aerogel achieves stable operation for over 500 hours in both PEMWE and AEMWE.<sup>175</sup> Meanwhile, the NHP-RuRuO<sub>x</sub> hollow porous structure demonstrates the great potential of 3D architectures for addressing both activity and stability challenges, even with an ultra-low precious metal loading of 0.108 mg cm<sup>-2</sup>.<sup>202</sup> However, these advantages do not come for free. The synthesis of 3D structures is often more complex, more costly, and harder to control for batch-to-batch consistency.

In summary, catalysts with different dimensions each have their own inherent limitations and suitable applications. There is no single "correct answer" that fits all industrial scenarios. 0D, 1D, 2D, and 3D structures each involve trade-offs in synthesis simplicity, mass transport efficiency, long-term stability, and cost control. A summary of the device performance of Ru-based catalysts with different dimensional structures is provided in Table 3. Therefore, the dimensional design of catalysts should follow a "scenario-driven" principle. For stationary large-scale electrolyzers that demand ultra-high stability, three-dimensional self-supported structures are the most reliable



View Article Online  
DOI: 10.1039/B55603774E

choice. For scenarios that prioritize large-scale production and cost efficiency, zero-dimensional nanoparticles still offer irreplaceable value. Future development of industrial catalysts should not only focus on optimizing intrinsic activity but also

pay more attention to matching electrode structures with actual operating conditions. Only then can we effectively bridge the gap from "materials design" to "system integration."

Table 3 Summary of Device Performance of Ru-Based Catalysts

Dimension	Sample	Device type	Test temperature	Potential	Stability	Refs.
0D	Pt-Ru/ZrO <sub>2</sub>	AEMWE	-	1.83V@1.0 A cm <sup>-2</sup>	150 h@1.0 A cm <sup>-2</sup>	202
0D	Pt-Ru <sub>fcc</sub>	AEMWE	80°C	1.82V@1.0 A cm <sup>-2</sup>	400 h@1.0 A cm <sup>-2</sup>	203
0D	Mn-RuO <sub>2</sub>	AEMWE	-	1.87V@1.0 A cm <sup>-2</sup>	-	103
0D	Pt-Ru(fcc)	PEMWE	65°C	1.61V@1.0 A cm <sup>-2</sup>	1000 h@1.0 A cm <sup>-2</sup>	204
0D	Ru/Cr <sub>2</sub> O <sub>3</sub>	AEMWE	80°C	1.65V@0.5 A cm <sup>-2</sup>	2000 h@0.5 A cm <sup>-2</sup>	205
0D	Pt <sub>1</sub> Cl <sub>0.5</sub> /Ru-NPs@RuO <sub>x</sub>	PEMWE	65°C	1.66V@1.0 A cm <sup>-2</sup>	1000 h@1.0 A cm <sup>-2</sup>	95
1D	Ru/WO <sub>x</sub>	AEMWE	60°C	1.89V@1.0 A cm <sup>-2</sup>	-	140
1D	Ru <sub>54</sub> -CoP	AEMWE	60°C	1.91V@1.0 A cm <sup>-2</sup>	160 h@1.5 A cm <sup>-2</sup>	125
1D	Li <sub>3.0</sub> RuSn <sub>0.8</sub> NWs	AEMWE	80°C	1.689V@1.0 A cm <sup>-2</sup>	1000 h@1.0 A cm <sup>-2</sup>	128
1D	Ru/S-Co <sub>3</sub> O <sub>4</sub>	AEMWE	70°C	1.98V@1.0 A cm <sup>-2</sup>	1300 h@1.0 A cm <sup>-2</sup>	206
1D	CoRuO <sub>x</sub> /Ru-Co <sub>3</sub> O <sub>4</sub>	PEMWE	25°C	1.71V@1.0 A cm <sup>-2</sup>	120 h@0.2 A cm <sup>-2</sup>	143
2D	Ru-CoP/MXene	AEMWE	25°C	1.75V@1.0 A cm <sup>-2</sup>	200 h@1.0 A cm <sup>-2</sup>	170
2D	(FeNiMoRuV)O <sub>2-x</sub>	AEMWE	-	1.923V@1.0 A cm <sup>-2</sup>	200 h@1.0 A cm <sup>-2</sup>	207
2D	S-RuO <sub>2</sub>	AEMWE	25°C	2.17V@0.5 A cm <sup>-2</sup>	100 h@0.4 A cm <sup>-2</sup>	208
2D	Ru-LC-Ni(OH) <sub>2</sub>	AEMWE	80°C	1.69V@1.0 A cm <sup>-2</sup>	500 h@0.5 A cm <sup>-2</sup>	209
2D	Ru-NiCr LDH	AEMWE	80°C	1.80V@1.8 A cm <sup>-2</sup>	100 h@0.5 A cm <sup>-2</sup>	210
3D	CeO <sub>2</sub> -Ru aerogel	PEMWE	25°C	1.78V@1.0 A cm <sup>-2</sup>	500 h@2.0 A cm <sup>-2</sup>	175
3D	PtNi/Ru	AEMWE	60°C	2.2V@1.0 A cm <sup>-2</sup>	250 h@0.25 A cm <sup>-2</sup>	211
3D	Ru-Ni <sub>3</sub> N	AEMWE	-	1.79V@1.0 A cm <sup>-2</sup>	550 h@0.5 A cm <sup>-2</sup>	182
3D	Ru/RuS <sub>2</sub> /RuO <sub>2</sub>	PEMWE	80°C	1.59V@1.0 A cm <sup>-2</sup>	100 h@0.1 A cm <sup>-2</sup>	212
3D	L-Ru/Co(OH) <sub>x</sub>	AEMWE	-	2.0V@1.68 A cm <sup>-2</sup>	500 h@1.68 A cm <sup>-2</sup>	199
3D	NHP-RuIrO <sub>x</sub>	PEMWE	-	1.60V@1.0 A cm <sup>-2</sup>	150 h@1.0 A cm <sup>-2</sup>	201
3D	NiRu-NH <sub>2</sub> BDC/NF	AEMWE	60°C	1.76V@0.5 A cm <sup>-2</sup>	100 h@0.5 A cm <sup>-2</sup>	189

## Conclusions

This review organizes ruthenium-based catalysts into categories based on the dimensional configuration of their metal-based supports (ranging from 0D particles to 3D frameworks) and offers a comparative assessment of their catalytic behavior under different electrolyte conditions (Table 4). Despite substantial advances achieved through the application of metal-based supports for modulating Ru-based hydrogen evolution catalysts, numerous challenges remain on the path from fundamental research to practical application. Based on a systematic review of 0D, 1D, 2D, and 3D supports, we propose future perspectives from three dimensions: precise synthesis, mechanistic understanding, and operational stability.

1) At the level of precise synthesis, achieving atomically controlled and cost-effective preparation for supports of different dimensionalities remains a core challenge. 0D supports require a balance between sub-nanometer size control and resistance to agglomeration; for 1D supports, strategies enabling the simultaneous modulation of crystal phase, defects, and surface functional groups need to be developed; while for 3D supports, Ru migration during high-temperature processing must be suppressed. Introducing the concept of the materials genome, combined with high-throughput experiments and machine learning-assisted parameter optimization, holds promise for accelerating the screening of optimal synthesis pathways tailored to different dimensionalities.

- 2) At the level of mechanistic understanding, current insights based on static characterization and single descriptors (such as  $\Delta G_{H^+}$ ) are insufficient to fully capture the multi-step reaction processes in complex electrolytes. In the future, it is necessary to develop multi-modal in-situ characterization techniques under operando conditions (such as XAS, ETEM, and Raman spectroscopy) to track the evolution of Ru oxidation states, dynamic behaviour, and interfacial adsorption configurations. For systems involving phase transitions, reconstruction, or hydrogen spillover, a direct correlation needs to be established among electronic structure, interfacial properties, and reaction kinetics to reveal the dynamic active centers under realistic conditions. Theoretical calculations should be extended from single final-state descriptions to full-pathway simulations, comprehensively considering multi-step energy barriers and environmental factors such as the interfacial electric field and solvation effects. Constructing a structure-activity relationship database encompassing support dimensionality, Ru species, and reaction conditions, integrated with artificial intelligence, can provide a data foundation for the high-throughput screening of catalysts.
- 3) At the level of operational stability, although numerous Ru-based catalysts exhibit excellent performance in laboratory settings, their long-term stability under industrial current densities, high temperatures, strong alkaline conditions, or in seawater environments remains a bottleneck. Concerning metal-based supports, oxides are prone to



reductive phase transitions, phosphides face the risk of leaching, and metal-organic frameworks are limited by their electrical conductivity and hydrolytic stability. Future efforts should focus on developing integrated electrodes to eliminate binder interfaces and exploring protective shell encapsulation strategies to inhibit Ru dissolution and support corrosion. Notably, in complex electrolyte systems such as seawater and neutral media, precise regulation of metal-support interactions serves as a viable approach for improving long-term stability. By constructing strong metal-support interactions, the electron transfer between the support and Ru can be harnessed to stabilize the oxidation state of Ru, thereby mitigating its dissolution and agglomeration under chloride ion attack. On the other hand, selecting an electrochemically stable support can prevent the corrosion and phase transformation of the support itself. Furthermore, the interfacial structure anchored by strong interactions enhances the anti-migration ability of Ru clusters and maintains the dynamic balance of interfacial water, thereby achieving high activity and long-term stability in both seawater and neutral media.

- 4) At the device level, catalyst evaluation should advance beyond half-cell tests toward practical operating conditions, such as those in anion exchange membrane electrolyzers. Three-electrode measurements in half-cells offer a rapid assessment of intrinsic activity. However, they fail to capture the mass transport, ohmic losses, and

membrane electrode assembly integration, that characterize real electrolyzers. Future efforts should prioritize the loading processes of catalysts within membrane electrode assemblies, their interfacial compatibility with ionomers, and their stability under high current densities. Validation under realistic device conditions—whether in anion exchange membrane or proton exchange membrane electrolyzers—is essential to accurately assess the practical potential of catalysts. Such steps are crucial for transitioning Ru-based catalysts from laboratory research toward industrial implementation.

In conclusion, Metal-based supports of different dimensions offer multi-scale tuning capabilities for Ru-based hydrogen evolution catalysts. 0D supports maximize atom utilization and quantum confinement effects. 1D supports provide anisotropic charge transport and opportunities for crystal phase engineering. 2D supports, with their high specific surface area and tunable electronic structure, enable uniform dispersion of active centers and interfacial synergy. 3D supports integrate the synergistic optimization of mass transport, electrical conductivity, and structural stability. In the future, innovations in synthesis methods, advancements in operando characterization, breakthroughs in theoretical calculations, and progress in device integration are anticipated to yield a new class of Ru-based catalysts combining high activity, robust stability, and cost-effectiveness. This will establish the material foundation for scaling up green hydrogen technologies

Table 4 Summary of metal-supported Ru-based catalysts for HER.

Dimension	Sample	Electrolyte	Overpotential	Refs.
0D	Pt-Ru	1.0 M KOH	14 mV@10 mA cm <sup>-2</sup>	83
0D	MgO <sub>x</sub> -Ru	1.0 M KOH	19 mV@10 mA cm <sup>-2</sup>	88
0D	Mn-RuO <sub>2</sub>	1.0 M KOH	16 mV@10 mA cm <sup>-2</sup>	103
0D	Ru/ac-CeO <sub>2-δ</sub>	1.0 M KOH	21.2 mV@10 mA cm <sup>-2</sup>	107
0D	Ru-ASN/Mn <sub>3</sub> O <sub>4</sub>	1.0 M PBS	8 mV@10 mA cm <sup>-2</sup>	115
0D	LaRuSi	1.0 M KOH	72 mV@10 mA cm <sup>-2</sup>	120
1D	Ru@Cu-TiO <sub>2</sub> /Cu	1.0 M NaOH	16 mV@10 mA cm <sup>-2</sup>	127
1D	PdH@Ru NBS	1.0 M KOH	14 mV@10 mA cm <sup>-2</sup>	132
1D	Ru/WO <sub>3</sub> -H	0.5 M H <sub>2</sub> SO <sub>4</sub>	43.8 mV@10 mA cm <sup>-2</sup>	139
1D	RWO-A	1.0 M KOH	37 mV@10 mA cm <sup>-2</sup>	140
1D	CoRuO <sub>x</sub> /Ru-Co <sub>3</sub> O <sub>4</sub>	0.5 M H <sub>2</sub> SO <sub>4</sub>	13.9 mV@10 mA cm <sup>-2</sup>	143
1D	RuCo/TiO <sub>2</sub> NTs	0.5 M H <sub>2</sub> SO <sub>4</sub>	17 mV@10 mA cm <sup>-2</sup>	147
2D	RuNi NSs	1.0 M KOH	48 mV@10 mA cm <sup>-2</sup>	150
2D	RuZn NSs	1.0 M KOH	11 mV@10 mA cm <sup>-2</sup>	152
2D	Ru <sub>2</sub> Co <sub>1-4</sub> @E-MoS <sub>2-x</sub> NSs	1.0 M KOH	36 mV@10 mA cm <sup>-2</sup>	164
2D	Pt,Ru,Rh,Pd,Re-MoSe <sub>2</sub>	0.5 M H <sub>2</sub> SO <sub>4</sub>	32 mV@10 mA cm <sup>-2</sup>	166
2D	Ru@Ti <sub>3</sub> C <sub>2</sub> T <sub>x</sub> -Vc	1.0 M KOH	32 mV@10 mA cm <sup>-2</sup>	169
2D	Ru/Mo <sub>2</sub> CT <sub>x</sub>	1.0 M PBS	73 mV@10 mA cm <sup>-2</sup>	172
3D	CeO <sub>2</sub> -Ru aerogel	1.0 M KOH	12.9 mV@10 mA cm <sup>-2</sup>	175
3D	Cr <sub>0.033</sub> Ru <sub>0.967</sub> fcc/hcp	1.0 M KOH	14 mV@10 mA cm <sup>-2</sup>	176
3D	Ru/c-Ti <sub>3</sub> C <sub>2</sub> T <sub>x</sub> /NF	1.0 M KOH	37 mV@10 mA cm <sup>-2</sup>	184
3D	FF-Na-Ru	1.0 M KOH	30 mV@10 mA cm <sup>-2</sup>	185
3D	NiFeRu <sub>5A+NP</sub> -DOBDC	1.0 M KOH	25 mV@10 mA cm <sup>-2</sup>	188
3D	NiRu-NH <sub>2</sub> BDC/NF	1.0 M KOH	21 mV@10 mA cm <sup>-2</sup>	189

## Author contributions

All of the authors contributed to the literature search, writing and editing of this review.

## Conflicts of interest

There are no conflicts to declare.



## Data availability statements

No primary research results, software or code have been included and no new data were generated or analysed as part of this review.

## Acknowledgements

This work was supported by the National Natural Science Foundation of China (21571038 and 22465009), Guizhou Province Department of Education (2021312) and Guizhou Province Department of Science and Technology (2019–5666).

## Notes and references

- E. T. C. Vogt and B. M. Weckhuysen, *Nature*, 2024, **629**, 295–306.
- P. D. Luna, C. Hahn, D. Higgins, S. A. Jaffer, T. F. Jaramillo and E. H. Sargent, *Science*, 2019, **364**, 350.
- F. Chang, W. Gao, J. Guo and P. Chen, *Adv. Mater.*, 2021, **33**, 2005721.
- S. Verhelst, J. W. G. Turner, L. Sileghem and J. Vancoillie, *Prog. Energy Combust. Sci.*, 2019, **70**, 43–88.
- T. Terlouw, C. Bauer, R. McKenna and M. Mazzotti, *Energy Environ. Sci.*, 2022, **15**, 3583–3602.
- J. Chi and H. Yu, *Chin. J. Catal.*, 2018, **39**, 390–394.
- A. Buttler and H. Spliethoff, *Renew. Sust. Energ. Rev.*, 2018, **82**, 2440–2454.
- Z. Li, L. Sun, Y. Zhang, Y. Han, W. Zhuang, L. Tian and W. Tan, *Coord. Chem. Rev.*, 2024, **510**, 215837.
- S. Anantharaj, S. Noda, V. R. Jothi, S. Yi, M. Driess and P. W. Menezes, *Angew. Chem. Int. Ed.*, 2021, **60**, 18981–19006.
- Z. Zhou, Z. Pei, L. Wei, S. Zhao, X. Jian and Y. Chen, *Energy Environ. Sci.*, 2020, **13**, 3185–3206.
- C. C. L. McCrory, S. Jung, I. M. Ferrer, S. M. Chatman, J. C. Peters and T. F. Jaramillo, *J. Am. Chem. Soc.*, 2015, **137**, 4347–4357.
- Y. Zheng, Y. Jiao, Y. Zhu, L. H. Li, Y. Han, Y. Chen, M. Jaroniec and S.-Z. Qiao, *J. Am. Chem. Soc.*, 2016, **138**, 16174–16181.
- Y. Yang, Y. Yu, J. Li, Q. Chen, Y. Du, P. Rao, R. Li, C. Jia, Z. Kang, P. Deng, Y. Shen and X. Tian, *Nano-Micro Lett.*, 2021, **13**, 160.
- Y. Zhu, K. Fan, C. S. Hsu, G. Chen, C. Chen, T. Liu, Z. Lin, S. She, L. Li, H. Zhou, Y. Zhu, H. M. Chen and H. Huang, *Adv. Mater.*, 2023, **35**, 2301133.
- P. Sun, R. Jiang, Z. Qiao, S. Huang, S. Wang and D. Cao, *Nat. Commun.*, 2025, **16**, 10617.
- Z. Liu, Y. Du, R. Yu, M. Zheng, R. Hu, J. Wu, Y. Xia, Z. Zhuang and D. Wang, *Angew. Chem. Int. Ed.*, 2022, **62**, e202212653.
- Y. Guo, S. Mei, K. Yuan, D.-J. Wang, H.-C. Liu, C.-H. Yan and Y.-W. Zhang, *ACS Catal.*, 2018, **8**, 6203–6215.
- P. Su, W. Pei, X. Wang, Y. Ma, Q. Jiang, J. Liang, S. Zhou, J. Zhao, J. Liu and G. Q. Lu, *Angew. Chem. Int. Ed.*, 2021, **60**, 16044–16050.
- K. Liu, X. Zhao, G. Ren, T. Yang, Y. Ren, A. F. Lee, Y. Su, X. Pan, J. Zhang, Z. Chen, J. Yang, X. Liu, T. Zhou, W. Xi, J. Luo, C. Zeng, H. Matsumoto, W. Liu, Q. Jiang, K. Wilson, A. Wang, B. Qiao, W. Li and T. Zhang, *Nat. Commun.*, 2020, **11**, 1263.
- J. Li, Z. Liu, D. A. Cullen, W. Hu, J. Huang, L. Yao, Z. Peng, P. Liao and R. Wang, *ACS Catal.*, 2019, **9**, 11088–11103.
- V. Ramalingam, P. Varadhan, H. C. Fu, H. Kim, D. Zhang, S. Chen, L. Song, D. Ma, Y. Wang, H. N. Alshareef and J. H. He, *Adv. Mater.*, 2019, **31**, 1903841.
- Y. Wang, X. Zheng and D. Wang, *Nano Res.*, 2021, **15**, 1730–1752.
- C. Zhan, Y. Xu, L. Bu, H. Zhu, Y. Feng, T. Yang, Y. Zhang, Z. Yang, B. Huang, Q. Shao and X. Huang, *Nat. Commun.*, 2021, **12**, 6261.
- D. Ma, C. Lai, H. Yi, X. Huo, L. Li, M. Zhang, F. Xu, H. Yan, S. Hu and Y. Luo, *Coord. Chem. Rev.*, 2025, **522**, 216241.
- L. Xu and Q. Yuan, *Chem. Commun.*, 2025, **61**, 12246–12264.
- F. Gao, Y. Zhang, Z. Wu, H. You and Y. Du, *Coord. Chem. Rev.*, 2021, **436**, 213825.
- J. Li, N. Wu, J. Zhang, H.-H. Wu, K. Pan, Y. Wang, G. Liu, X. Liu, Z. Yao and Q. Zhang, *Nano-Micro Lett.*, 2023, **15**, 227.
- S. M. Ghoreishian, K. Shariati, Y. S. Huh and J. Lauterbach, *Chem. Eng. J.*, 2023, **467**, 143533.
- S. Biswas, S. Barth and J. D. Holmes, *Nano Res.*, 2017, **10**, 1510–1523.
- P. Wang, K. Jiang, G. Wang, J. Yao and X. Huang, *Angew. Chem. Int. Ed.*, 2016, **55**, 12859–12863.
- Z. Liu, L. Zeng, J. Yu, L. Yang, J. Zhang, X. Zhang, F. Han, L. Zhao, X. Li, H. Liu and W. Zhou, *Nano Energy*, 2021, **85**, 105940.
- X. Yu, Y. Li, C. Pei, Y. Lu, J. K. Kim, H. S. Park and H. Pang, *Adv. Sci.*, 2024, **11**, 2310013.
- M. Bat - Erdene, M. Batmunkh, B. Sainbileg, M. Hayashi, A. S. R. Bati, J. Qin, H. Zhao, Y. L. Zhong and J. G. Shapter, *Small*, 2021, **17**, 2102218.
- T. T. Zhou, K. Y. Dong, Z. Zheng and Q. Yuan, *Rare Met.*, 2025, **44**, 3119–3129.
- D. Wang, R. Su, C. Han, C. Cui, R. Wang, L. Xiong, H. Zhang, P. Xiao, G. Chen, S. Hao, S. Zhi, S. Lee and Y. Yang, *Small*, 2026, <https://doi.org/10.1002/smll.202513391>.
- D. Wang, W. Liu, H. Wang, S. Lu, Y. Li, L. Luo, L. Yu and Y. Xiang, *Chem. Eng. J.*, 2024, **485**, 149807.
- J. Yin, T. Lu, J. Li, J. Liu, Y. Lin, D. Sun, L. Xu, Q. Zhao, H. Pang, S. Zhang and Y. Tang, *Adv. Funct. Mater.*, 2024, **35**, 2417034.
- L. M. Cao, L. H. Yu, H. B. Huang, C. J. Gao, X. Huang, X. F. Zhang, X. H. Zhang, Z. Y. Du and C. T. He, *Adv. Functional Mater.*, 2024, **34**, 2411111.
- W. Wu, S. Yang, H. Qian, L. Zhang, L. Peng, L. Li, B. Liu and Z. Wei, *Chin. J. Catal.*, 2024, **66**, 1–19.
- H. Wang, Y. Yang, F. J. DiSalvo and H. D. Abruña, *ACS Catal.*, 2020, **10**, 4608–4616.
- H. Zhang, J. Li, H. Yan, X. Chen and H. Fu, *Adv. Mater.*, 2025, **38**, e16207.
- X. Cao, J. Huo, L. Li, J. Qu, Y. Zhao, W. Chen, C. Liu, H. Liu and G. Wang, *Adv. Energy Mater.*, 2022, **12**, 2202119.
- Y. Liu, Q. Wang, J. Zhang, J. Ding, Y. Cheng, T. Wang, J. Li, F. Hu, H. B. Yang and B. Liu, *Adv. Energy Mater.*, 2022, **12**, 2200928.
- J. Ding, X. Jiang, C. Wang, Z. Zhu, C. Xu, Y. Zhou, X. Wang, Q. Liu, Z. Liu, Y. Tang, J. Lin and G. Fu, *J. Energy Chem.*, 2023, **86**, 510–517.
- J. Wang, M. Zhou, R. Fu, J. Ge, W. Yang, X. Hong, C. Sun, X. Liao, Y. Zhao and Z. Wang, *Adv. Funct. Mater.*, 2024, **34**, 2315236.
- Y.-N. Zhou, F.-L. Wang, J. Nan, B. Dong, H.-Y. Zhao, F.-G. Wang, N. Yu, R.-N. Luan, D.-P. Liu and Y.-M. Chai, *Appl. Catal. B: Environ.*, 2022, **304**, 120917.
- A. Jacob-Villedieu, S. Katipamula, A. Marchand, B. Reuillard, V. Artero, V. Fourmond, B. Faure, A. J. Simaan and C. Léger, *J. Am. Chem. Soc.*, 2025, **147**, 39391–39400.
- X. Zhang, L. Wang, Y. Xie and H. Fu, *Coord. Chem. Rev.*, 2025, **533**, 216560.
- F. Sun, Q. Tang and D.-e. Jiang, *ACS Catal.*, 2022, **12**, 8404–8433.
- F. Bao, E. Kemppainen, I. Dorbandt, R. Bors, F. Xi, R. Schlatmann, R. van de Krol and S. Calnan, *ChemElectroChem*, 2021, **8**, 195–208.
- X. Wang, Y. Zheng, W. Sheng, Z. J. Xu, M. Jaroniec and S.-Z. Qiao, *Mater. Today*, 2020, **36**, 125–138.



- 52 C. Hu, L. Zhang and J. Gong, *Energy Environ. Sci.*, 2019, **12**, 2620-2645.
- 53 S. Zhao, Z. X. Li, H. T. Guo, J. Li, Z. L. Liu, P. F. Wang, L. L. Wang and T. F. Yi, *Adv. Funct. Mater.*, 2025, **36**, e09799.
- 54 F. Li, G. F. Han, H. J. Noh, I. Ahmad, I. Y. Jeon and J. B. Baek, *Adv. Mater.*, 2018, **30**, 1803676.
- 55 W. Zhou, J. Jia, J. Lu, L. Yang, D. Hou, G. Li and S. Chen, *Nano Energy*, 2016, **28**, 29-43.
- 56 Y. Li, H. Wang, L. Xie, Y. Liang, G. Hong and H. Dai, *J. Am. Chem. Soc.*, 2011, **133**, 7296-7299.
- 57 T. F. Jaramillo, K. P. Jørgensen, J. Bonde, J. H. Nielsen, S. Horch and I. Chorkendorf, *Science*, 2007, **317**, 100-102.
- 58 A. J. Medford, A. Vojvodic, J. S. Hummelshøj, J. Voss, F. Abild-Pedersen, F. Studt, T. Bligaard, A. Nilsson and J. K. Nørskov, *J. Catal.*, 2015, **328**, 36-42.
- 59 Y.-J. Zhang, V. Sethuraman, R. Michalsky and A. A. Peterson, *ACS Catal.*, 2014, **4**, 3742-3748.
- 60 E. Skúlason, V. Tripkovic, M. E. Björketun, S. d. Gudmundsdóttir, G. Karlberg, J. Rossmeisl, T. Bligaard, H. Jónsson and J. K. Nørskov, *J. Phys. Chem. C*, 2010, **114**, 18182-18197.
- 61 S. Ye, F. Liu, F. She, J. Chen, D. Zhang, A. Kumatani, H. Shiku, L. Wei and H. Li, *Angew. Chem. Int. Ed.*, 2025, **64**, e202425402.
- 62 D. Guan, H. Xu, Q. Zhang, Y. C. Huang, C. Shi, Y. C. Chang, X. Xu, J. Tang, Y. Gu, C. W. Pao, S. C. Haw, J. M. Chen, Z. Hu, M. Ni and Z. Shao, *Adv. Mater.*, 2023, **35**, 2305074.
- 63 C. D. Zeinalipour-Yazdi and R. A. v. Santen, *J. Phys. Chem. A*, 2009, **113**, 6971-6978.
- 64 L. Xiang, P. Zhang, C. Liu, X. He, H. B. Li, Y. Li, Z. Wang, J. Hihath, S. H. Kim, D. N. Beratan and N. Tao, *Matter*, 2020, **3**, 166-179.
- 65 I. T. McCrum and M. T. M. Koper, *Nat. Energy*, 2020, **5**, 891-899.
- 66 Z. Chen, Y. Song, J. Cai, X. Zheng, D. Han, Y. Wu, Y. Zang, S. Niu, Y. Liu, J. Zhu, X. Liu and G. Wang, *Angew. Chem. Int. Ed.*, 2018, **57**, 5076-5080.
- 67 P. Kuang, Z. Ni, B. Zhu, Y. Lin and J. Yu, *Adv. Mater.*, 2023, **35**, 2303030.
- 68 N. Acerbi, S. C. E. Tsang, G. Jones, S. Golunski and P. Collier, *Angew. Chem. Int. Ed.*, 2013, **52**, 7737-7741.
- 69 A. Nilsson, L. G. M. Pettersson, B. Hammer, T. Bligaard, C. H. Christensen and J. K. Nørskov, *Catal. Lett.*, 2005, **100**, 111-114.
- 70 B. HAMMER and J. K. NØRSKOV, *Adv. Catal.*, 2000, **45**, 71-129.
- 71 S. Jiao, X. Fu and H. Huang, *Adv. Funct. Mater.*, 2021, **32**, 2107651.
- 72 Y. Zhang, Y. Wang, N. Ma, B. Liang, Y. Xiong and J. Fan, *Small*, 2023, **20**, 2306840.
- 73 J. K. Nørskov, F. Abild-Pedersen, F. Studt and T. Bligaard, *Proc. Natl. Acad. Sci.*, 2011, **108**, 937-943.
- 74 Z. Yang, T. Xu, H. Li, M. She, J. Chen, Z. Wang, S. Zhang and J. Li, *Chem. Rev.*, 2023, **123**, 11047-11136.
- 75 C. Durante, *Curr. Opin. Electrochem.*, 2022, **36**, 101119.
- 76 Z. Li, R. Wu, L. Zhao, P. Li, X. Wei, J. Wang, J. S. Chen and T. Zhang, *Nano Res.*, 2021, **14**, 3795-3809.
- 77 J. Shan, C. Ye, Y. Jiang, M. Jaroniec, Y. Zheng and S.-Z. Qiao, *Sci. Adv.*, 2022, **8**, eabo0762.
- 78 Y. Liu, S. Roy, S. Sarkar, J. Xu, Y. Zhao and J. Zhang, *Carbon Energy*, 2021, **3**, 795-826.
- 79 K. Ren, Z. Liu, T. Wei and Z. Fan, *Nano-Micro Letters*, 2021, **13**.
- 80 M. Ha, J.-H. Kim, M. You, Q. Li, C. Fan and J.-M. Nam, *Chem. Rev.*, 2019, **119**, 12208-12278.
- 81 D. Pedone, M. Moglianetti, E. De Luca, G. Bardi and P. P. Pompa, *Chem. Soc. Rev.*, 2017, **46**, 4951-4975.
- 82 J. W. M. Crawley, I. E. Gow, N. Lawes, I. Kowalec, L. Kaban, C. R. A. Catlow, A. J. Logsdail, S. H. Taylor, N. F. Dummer and G. J. Hutchings, *Chem. Rev.*, 2022, **122**, 6795-6849.
- 83 Q. Li, S. Cheong, A. R. Poerwoprajitno, S. Xiang, A. I. Frenkel, Y. Yang, N. M. Bedford, S. Umer, M. Lessio, I. Ohnishi, Z. R. Ramadhan, D. L. Huber, L. Dai, W. Schuhmann, J. J. Gooding and R. D. Tilley, *Adv. Mater.*, 2025, **37**, e09610.
- 84 Y. Xie, Y. Feng, S. Pan, H. Bao, Y. Yu, F. Luo and Z. Yang, *Adv. Funct. Mater.*, 2024, **34**, 2406351.
- 85 H. Wang, Y. Yang, F. J. DiSalvo and H. D. Abruña, *ACS Catal.*, 2020, **10**, 4608-4616.
- 86 Y. Jiang, Y. Mao, Y. Jiang, H. Liu, W. Shen, M. Li and R. He, *Chem. Eng. J.*, 2022, **450**, 137909.
- 87 X. Qin, L. Zhang, G.-L. Xu, S. Zhu, Q. Wang, M. Gu, X. Zhang, C. Sun, P. B. Balbuena, K. Amine and M. Shao, *ACS Catal.*, 2019, **9**, 9614-9621.
- 88 X. Gu, Z. Li, H. Jang, J. Tang, C. Sun, M. G. Kim, S. Liu, X. Liu and L. Hou, *Small*, 2025, **21**, 2412123.
- 89 L. Hou, Z. Li, H. Jang, Y. Wang, X. Cui, X. Gu, M. G. Kim, L. Feng, S. Liu and X. Liu, *Adv. Energy Mater.*, 2023, **13**, 2300177.
- 90 Y. Wang, J. Li, P. Yang, H. Li, G. Xu, Y. Du, C. Li, W. Jin, T. Ma, Z. Wu and L. Wang, *J. Energy Chem.*, 2025, **102**, 618-627.
- 91 Z. J. Guan, J. J. Li, F. Hu and Q. M. Wang, *Angew. Chem. Int. Ed.*, 2022, **61**, e202209725.
- 92 G. Sun, Y. Xu, Y. Xia, D. Kong, J. Zhu, D. Li, X. Liu, J. Lai, J. Chi and L. Wang, *Adv. Funct. Mater.*, 2025, **36**, e12343.
- 93 L.-W. Shen, Y. Wang, L. Shen, J.-B. Chen, Y. Liu, M.-X. Hu, W.-Y. Zhao, K.-Y. Xiong, S.-M. Wu, Y. Lu, J. Ying, M. M. Titirici, C. Janiak, G. Tian and X.-Y. Yang, *Energy Environ. Sci.*, 2024, **17**, 3888-3897.
- 94 Z. Yuehuan and Q. Yuan, *Chem. Commun.*, 2024, **60**, 7188-7191.
- 95 Q. Wang, W. Ling, Y. Lu, H. Zhao, Q. Cheng, Y. Huang, L. Zu, B. Yang and H. Yang, *Angew. Chem. Int. Ed.*, 2025, **64**, e202506619.
- 96 H. Wang, C. Zhang, D. Zhang, L. Jiang, Y. Gao, T. Zhuang and Z. Lv, *Small*, 2024, **20**, 2403170.
- 97 Y. Zhang and Q. Yuan, *Chemical Science*, 2026, **17**, 2827-2836.
- 98 H. Ling, Q. Yuan, T. Sheng and X. Wang, *J. Colloid Interface Sci.*, 2025, **685**, 371-381.
- 99 Y. Dang, T. Wu, H. Tan, J. Wang, C. Cui, P. Kerns, W. Zhao, L. Posada, L. Wen and S. L. Suib, *Energy Environ. Sci.*, 2021, **14**, 5433-5443.
- 100 S. Dong, P. Wang, Z. Li, L. Wei, S. Liu, Y. Yang and F. Zheng, *Adv. Funct. Mater.*, 2024, **35**, 2422166.
- 101 Y. Zhu, M. Klingenhof, C. Gao, T. Koketsu, G. Weiser, Y. Pi, S. Liu, L. Sui, J. Hou, J. Li, H. Jiang, L. Xu, W.-H. Huang, C.-W. Pao, M. Yang, Z. Hu, P. Strasser and J. Ma, *Nat. Commun.*, 2024, **15**, 1447.
- 102 X. Zhang, Z. Su, D. Xiang, W. Xu, Q. Guo, Y. Fan, X. Kang, Y. Sheng, F. Zheng and W. Chen, *Adv. Funct. Mater.*, 2024, **34**, 2409306.
- 103 Q. Li, Q. Xu, Z. Pei, Z. Zhang, W. Xu, J. Mao, Q. Shang, Y. Ni, Y. Chen, Y. Chen, X. Liu, X. Li, Q. Zhang and N. Yang, *Adv. Energy Mater.*, 2025, **16**, 2500815.
- 104 T. Liu, L. Wang, B. Chen, H. Liu, S. Wang, Y. Feng, J. Zhang, Y. Yin and M. D. Guiver, *Angew. Chem. Int. Ed.*, 2025, **64**, e202421869.
- 105 Y. Shen, F. Liu, W. Li, L. Xin, H. Li, W. Xiao, G. Xu, D. Chen, C. Li, Y. Du, J. Wang, Z. Wu and L. Wang, *Chem. Eng. J.*, 2024, **495**, 153251.
- 106 C. Yang, Z. Wu, Z. Zhao, Y. Gao, T. Ma, X. Luo, C. Cheng, Y. Wang, S. Li and C. Zhao, *Adv. Mater.*, 2023, **35**, 2303331.
- 107 Q. Qin, H. Jang, X. Jiang, L. Wang, X. Wang, M. G. Kim, S. Liu, X. Liu and J. Cho, *Angew. Chem. Int. Ed.*, 2023, **63**, e202317622.
- 108 S. Zhao, S.-F. Hung, L. Deng, W.-J. Zeng, T. Xiao, S. Li, C.-H. Kuo, H.-Y. Chen, F. Hu and S. Peng, *Nat. Commun.*, 2024, **15**, 2728.
- 109 C. L. Bassani, G. van Anders, U. Banin, D. Baranov, Q. Chen, M. Dijkstra, M. S. Dimitriyev, E. Efrati, J. Farauto, O. Gang, N. Gaston, R. Golestani, G. I. Guerrero-Garcia, M. Gruenwald, A. Haji-Akbari, M. Ibáñez, M. Karg, T. Kraus, B. Lee, R. C. Van



- Lehn, R. J. Macfarlane, B. M. Moggetti, A. Nikoubashman, S. Osat, O. V. Prezhdo, G. M. Rotskoff, L. Saiz, A.-C. Shi, S. Skrabalak, I. I. Smalyukh, M. Tagliazucchi, D. V. Talapin, A. V. Tkachenko, S. Tretiak, D. Vaknin, A. Widmer-Cooper, G. C. L. Wong, X. Ye, S. Zhou, E. Rabani, M. Engel and A. Travesset, *ACS Nano*, 2024, **18**, 14791-14840.
- 110 Y.-Y. Ma, C.-X. Wu, X.-J. Feng, H.-Q. Tan, L.-K. Yan, Y. Liu, Z.-H. Kang, E.-B. Wang and Y.-G. Li, *Energy Environ. Sci.*, 2017, **10**, 788-798.
- 111 T. Liu, Y. Chen, X. Wang, Y. Di, K. Müllen, Z. Zhang and F. Wang, *Adv. Mater.*, 2025, **37**, 2417621.
- 112 C. Xu, H. Yu, H. Huang, S. Li, Y. Cao, W. Peng, Y. Li, H. Ke, S. Xu, H. Mo, C. Wu, H. Wang, Y. Zhang, X. Li and W. Chen, *Angew. Chem. Int. Ed.*, 2025, **64**, e202504667.
- 113 J. Z. Jiang, Z. Liu, C. Chen, Z. Li, M. G. Kim, C. Huang, H. Jang, X. Liu, S. Liu and L. Hou, *Adv. Energy Mater.*, 2025, **16**, e04762.
- 114 W. Shen, Q. Fu, C. S. Tsang, L. W. Wong, X. Zheng, J. Zhao and T. H. Ly, *Adv. Funct. Mater.*, 2024, **35**, 2406708.
- 115 L. Wan, H. Wang, B. Zeng, W. Wang, X. Liu, L. Cao, Y. Hu, Z. Cui and B. Dong, *Energy Environ. Sci.*, 2025, **18**, 4262-4275.
- 116 J. Kim, H. J. Kim, B. Ruqia, M. J. Kim, Y. J. Jang, T. H. Jo, H. Baik, H. S. Oh, H. S. Chung, K. Baek, S. Noh, M. Jung, K. j. Kim, H. K. Lim, Y. S. Youn and S. I. Choi, *Adv. Mater.*, 2021, **33**, 2105248.
- 117 L. Li, C. Liu, S. Liu, J. Wang, J. Han, T.-S. Chan, Y. Li, Z. Hu, Q. Shao, Q. Zhang and X. Huang, *ACS Nano*, 2022, **16**, 14885-14894.
- 118 J. Xu, C. Wang, M. Su, C. Zhang, F. Gao, X. Zhang and Q. Lu, *Adv. Funct. Mater.*, 2025, **36**, e15147.
- 119 H. Chen, X. Ai, W. Liu, Z. Xie, W. Feng, W. Chen and X. Zou, *Angew. Chem. Int. Ed.*, 2019, **58**, 11409-11413.
- 120 S. Shen, Z. Hu, H. Zhang, K. Song, Z. Wang, Z. Lin, Q. Zhang, L. Gu and W. Zhong, *Angew. Chem. Int. Ed.*, 2022, **61**, e202206460.
- 121 H. Zhang, K. Song, Z. Lin, Z. Wang, L. Zhang, S. Shen, L. Gu and W. Zhong, *Adv. Funct. Mater.*, 2024, **34**, 2405897.
- 122 L. Hou, Z. Li, H. Jang, M. G. Kim, J. Cho, W. Zhong, S. Liu and X. Liu, *Angew. Chem. Int. Ed.*, 2025, **64**, e202423756.
- 123 Y. Feng and Q. Yuan, *Chem. Commun.*, 2026, **62**, 1596-1600.
- 124 W. Zhao, D. Huang, Q. Yuan and X. Wang, *Nano Res.*, 2016, **9**, 3066-3074.
- 125 J. Sun, J. Zhang, J. Sun, Y. R. Hao, H. Xue, H. Dong, Z. Zhao and Q. Wang, *Adv. Funct. Mater.*, 2025, **36**, e23596.
- 126 B. Pang, S. Feng, Y. Xu, H. Chen, J. Li, Y. Yuan, X. Zou, X. Tian and Z. Kang, *Adv. Funct. Mater.*, 2024, **34**, 2411062.
- 127 Y. Zuo, S. Bellani, G. Saleh, M. Ferri, D. V. Shinde, M. I. Zappia, J. Buha, R. Brescia, M. Prato, R. Pascazio, A. Annamalai, D. O. de Souza, L. De Trizio, I. Infante, F. Bonaccorso and L. Manna, *J. Am. Chem. Soc.*, 2023, **145**, 21419-21431.
- 128 J. Mao, J. Liang, Y. Li, X. Liu, F. Ma, S. Liu, H. Ouyang, Z. Cai, T. Wang, Y. Zhao, Y. Huang and Q. Li, *J. Am. Chem. Soc.*, 2025, **147**, 7711-7720.
- 129 R. Jiang, D. T. Tran, J. Li and D. Chu, *Energy Environ. Mater.*, 2019, **2**, 201-208.
- 130 J. Li, X. Wang, J. Yu, K. Xu, Z. Jia, H. Li, L. Ren, Y. Yang, K. Chang, Y. Li, X. Liu, J. Lu and S. Liu, *Adv. Sci.*, 2025, **12**, 2501976.
- 131 X. Cao, L. Gao, J. Qu, L. Li, Y. Xie, Y. Zhao, G. Wang and H. Liu, *Small*, 2023, **19**, 2302639.
- 132 X. Jiang, Y. Wang, J. Ding, C. Wang, Y. Tang, Y. Cao, W. Wang and G. Fu, *Adv. Funct. Mat.*, 2024, **35**, 2414593.
- 133 S. Geng, R. Ren, R. Qin, N. Chen, J. Song, Z. Zheng, W. H. Huang, C. W. Pao, Z. Hu, L. Zhuang, X. Huang and L. Bu, *Adv. Mater.*, 2025, **38**, e17683.
- 134 R. Chen, T. Shu, F. Zhao, Y. Li, X. Yang, J. Li, D. Zhang, L.-Y. Gan, K. X. Yao and Q. Yuan, *Nano Res.*, 2022, **15**, 9010-9018.
- 135 Q. Yang, C. Zhang, B. Dong, Y. Cui, F. Wang, J. Cai, P. Jin and L. Feng, *Appl. Catal. B: Environ.*, 2021, **296**, 120359.
- 136 J. Chen, C. Chen, M. Qin, B. Li, B. Lin, Q. Mao, H. Yang, B. Liu and Y. Wang, *Nat. Commun.*, 2022, **13**, 5382.
- 137 J. Cai, W. Zhang, Y. Liu, R. Shen, X. Xie, W. Tian, X. Zhang, J. Ding, Y. Liu and B. Li, *Appl. Catal. B: Environ.*, 2024, **343**, 123502.
- 138 H. Liu, G. Tan, M. Li, Z. Zhang, M. Getaye Sendeku, Y. Li, Y. Kuang and X. Sun, *Chem. Eng. J.*, 2023, **458**, 141414.
- 139 J. Xu, F. Yang, X. Guo, S. Wang and L. Feng, *Journal of Energy Chemistry*, 2025, **105**, 170-177.
- 140 Z. Zhao, Y. Chen, Y. Liu, S. Qin, Z. Li, Z. Zhang and X. Meng, *Adv. Funct. Mater.*, 2025, **36**, e28280.
- 141 J.-X. Guo, D.-Y. Yan, K.-W. Qiu, C. Mu, D. Jiao, J. Mao, H. Wang and T. Ling, *J. Energy Chem.*, 2019, **37**, 143-147.
- 142 H. Huang, H. Jung, C.-Y. Park, S. Kim, A. Lee, H. Jun, J. Choi, J. W. Han and J. Lee, *Appl. Catal. B: Environ.*, 2022, **315**, 121554.
- 143 J. Wang, D. Wang, Y. Xiang, W. Yue, M. Sun, J. Sun and J. Li, *Nano Energy*, 2025, **145**, 111452.
- 144 K. Wang, Q. Chen, Y. Hu, W. Wei, S. Wang, Q. Shen and P. Qu, *Small*, 2018, **14**, 1802132.
- 145 S. Nong, W. Dong, J. Yin, B. Dong, Y. Lu, X. Yuan, X. Wang, K. Bu, M. Chen, S. Jiang, L.-M. Liu, M. Sui and F. Huang, *J. Am. Chem. Soc.*, 2018, **140**, 5719-5727.
- 146 S. M. Thalluri, J. Rodriguez - Pereira, J. Michalicka, E. Kolíbalová, L. Hromadko, S. Slang, M. Pouzar, H. Sopha, R. Zazpe and J. M. Macak, *Energy Environ. Mater.*, 2025, **8**, e12864.
- 147 H. Chen, Z. Gao, S. Ren, R. T. Gao, L. Wu and L. Wang, *Adv. Energy Mater.*, 2024, **15**, 2403067.
- 148 L. Li, S. Liu, C. Zhan, Y. Wen, Z. Sun, J. Han, T.-S. Chan, Q. Zhang, Z. Hu and X. Huang, *Energy Environ. Sci.*, 2023, **16**, 157-166.
- 149 J. Ding, Q. Shao, Y. Feng and X. Huang, *Nano Energy*, 2018, **47**, 1-7.
- 150 G. Liu, W. Zhou, B. Chen, Q. Zhang, X. Cui, B. Li, Z. Lai, Y. Chen, Z. Zhang, L. Gu and H. Zhang, *Nano Energy*, 2019, **66**, 104173.
- 151 Q. Yao, B. Huang, N. Zhang, M. Sun, Q. Shao and X. Huang, *Angew. Chem. Int. Ed.*, 2019, **58**, 13983-13988.
- 152 R. Yu, X. Cao, Q. Chen, W. Li, A. Huang, X. Wei and J. Mao, *Small*, 2023, **19**, 2303440.
- 153 V. Jose, V. H. Do, P. Prabhu, C. K. Peng, S. Y. Chen, Y. Zhou, Y. G. Lin and J. M. Lee, *Adv. Energy Mater.*, 2023, **13**, 2301119.
- 154 X. Jin, S. J. Kwon, M. G. Kim, M. Kim and S.-J. Hwang, *ACS Nano*, 2024, **18**, 15194-15203.
- 155 K. Deng, J. Yu, Q. Mao, R. Yang, H. Yu, Z. Wang, J. Wang, L. Wang and H. Wang, *Adv. Funct. Mater.*, 2025, **35**, 2420728.
- 156 J. Zhu, Y. Guo, F. Liu, H. Xu, L. Gong, W. Shi, D. Chen, P. Wang, Y. Yang, C. Zhang, J. Wu, J. Luo and S. Mu, *Angew. Chem. Int. Ed.*, 2021, **60**, 12328-12334.
- 157 K. Wang, J. Zhou, M. Sun, F. Lin, B. Huang, F. Lv, L. Zeng, Q. Zhang, L. Gu, M. Luo and S. Guo, *Adv. Mater.*, 2023, **35**, 2300980.
- 158 X. Xiao, Y. Shen, W. Xi, L. Gu, X. Li, B. Xi, S. Xiong and C. An, *Angew. Chem. Int. Ed.*, 2025, **64**, e202502927.
- 159 A. E. Russell, *Faraday Discuss.*, 2009, **140**, 9-10.
- 160 J. Zhang, X. Xu, L. Yang, D. Cheng and D. Cao, *Small Methods*, 2019, **3**, 1900653.
- 161 J. Wang, W. Fang, Y. Hu, Y. Zhang, J. Dang, Y. Wu, B. Chen, H. Zhao and Z. Li, *Appl. Catal. B: Environ.*, 2021, **298**, 120490.
- 162 J. Ge, D. Zhang, Y. Qin, T. Dou, M. Jiang, F. Zhang and X. Lei, *Appl. Catal. B: Environ.*, 2021, **298**, 120557.
- 163 J. Cai, J. Ding, D. Wei, X. Xie, B. Li, S. Lu, J. Zhang, Y. Liu, Q. Cai and S. Zang, *Adv. Energy Mater.*, 2021, **11**, 2100141.



- 164 R. Su, T. Ding, H. Tang, X. Yang, J. Zhang, X. Liu, J. Jia, Y. Liu, J. Ge, Z. Wu, Z. Dong and X. Zhu, *Adv. Sci.*, 2025, **13**, e19323.
- 165 H. Yue, Z. Guo, Z. Zhou, X. Zhang, W. Guo, S. Zhen, P. Wang, K. Wang and W. Yuan, *Angew. Chem. Int. Ed.*, 2024, **63**, e202409465.
- 166 Z. Luo, Y. Guo, C. He, Y. Guan, L. Zhang, Y. Li, Q. Zhang, C. He, X. Sun and X. Ren, *Angew. Chem. Int. Ed.*, 2024, **63**, e202405017.
- 167 M. Naguib, M. Kurtoglu, V. Presser, J. Lu, J. Niu, M. Heon, L. Hultman, Y. Gogotsi and M. W. Barsoum, *Adv. Mater.*, 2011, **23**, 4248-4253.
- 168 Y. Mao, X. Yang, K. Dong, T. Sheng and Q. Yuan, *J. Colloid Interface Sci.*, 2024, **662**, 208-217.
- 169 X. Wang, J. Ding, W. Song, X. Yang, T. Zhang, Z. Huang, H. Wang, X. Han and W. Hu, *Adv. Energy Mater.*, 2023, **13**, 2300148.
- 170 X. Liu, Y. Han, J. Liu, Y. Fu, X. Wang and Z. Ren, *Chem. Eng. J.*, 2025, **526**, 171299.
- 171 J. Li, C. Hou, C. Chen, W. Ma, Q. Li, L. Hu, X. Lv and J. Dang, *ACS Nano*, 2023, **17**, 10947-10957.
- 172 Y. Wu, L. Wang, T. Bo, Z. Chai, J. K. Gibson and W. Shi, *Adv. Funct. Mater.*, 2023, **33**, 2214375.
- 173 X. Yang, K. x. Yao, J. Y. Ye, Q. Yuan, F. Zhao, Y. Li and Z. Zhou, *Adv. Funct. Mater.*, 2021, **31**, 2103671.
- 174 S. Yan, W. Liao, M. Zhong, W. Li, C. Wang, N. Pinna, W. Chen and X. Lu, *Appl. Catal. B: Environ. Energy*, 2022, **307**, 121199.
- 175 H. Fan, X. Wan, S. Sun, X. Zhou, X. Bu, J. Ye, R. Bai, H. Lou, Y. Chen, J. Gao, J. Zhang, W. Gao and D. Wen, *Adv. Energy Mater.*, 2025, **15**, 2405681.
- 176 Y. Liu, L. Wang, V. Shamraienko, F. Röder, A. Wrzesińska - Lashkova, Y. Vaynzof, X. Zhang and A. Eychmüller, *Angew. Chem. Int. Ed.*, 2025, **64**, e202513970.
- 177 H. Chen, R. Ding, Z. W. Zeng, X. X. Jia, Y. C. Zhang, B. W. Liu, F. R. Zeng, Y. Z. Wang and H. B. Zhao, *Adv. Funct. Mater.*, 2025, **35**, 2505802.
- 178 H. Sun, Z. Yan, F. Liu, W. Xu, F. Cheng and J. Chen, *Adv. Mater.*, 2019, **32**, 1806326.
- 179 H. Sun, B. Yao, Y. Han, L. Yang, Y. Zhao, S. Wang, C. Zhong, J. Chen, C. P. Li and M. Du, *Adv. Energy Mater.*, 2024, **14**, 2303563.
- 180 H. Zhang, H. Guo, J. Ren, X. Jin, X. Li and R. Song, *Chem. Eng. J.*, 2021, **426**, 131300.
- 181 H. Yang, X. Long, F. Liu, J. Zhou, N. Chen, R. Feng, Y. Zhang, X.-Z. Fu, J.-L. Luo and B. Zhao, *Appl. Catal. B: Environ. Energy*, 2025, **366**, 125037.
- 182 L. Qiu, F. Tian, L. He, M. Li, F. Lin, L. Li, X. Ren, F. Wu, L. Li, T. Zhang, J. Sheng, Y. Yu, W. Yang and S. Guo, *Adv. Mater.*, 2025, **38**, e12568.
- 183 L. Guo, T. Liu, L. Zhang, M. Ma, P. Gao, D. Cao and D. Cheng, *Adv. Energy Mater.*, 2024, **15**, 2402558.
- 184 A. Kong, M. Peng, H. Gu, S. Zhao, Y. Lv, M. Liu, Y. Sun, S. Dai, Y. Fu, J. Zhang and W. Li, *Chem. Eng. J.*, 2021, **426**, 131234.
- 185 Z. Wu, Y. Zhao, H. Wu, Y. Gao, Z. Chen, W. Jin, J. Wang, T. Ma and L. Wang, *Adv. Funct. Mater.*, 2021, **31**, 2010437.
- 186 C. Liu, J. Wang, J. Wan and C. Yu, *Coord. Chem. Rev.*, 2021, **432**, 213743.
- 187 L. Deng, F. Hu, M. Ma, S. C. Huang, Y. Xiong, H. Y. Chen, L. Li and S. Peng, *Angew. Chem. Int. Ed.*, 2021, **60**, 22276-22282.
- 188 D. Li, M. Chen, D. Liu, C. Shen, H. Sun, Y. Zhang, T. He, Q. Lu, B. Li, T. Zhou, B. Wang, Y. Wu, G. Na, Y. Chen, J. Zhao, Y. Zhang, J. Zhang, F. Liu, H. Cui and Q. Liu, *Adv. Energy Mater.*, 2024, **15**, 2404714.
- 189 Z. Zhang, X. Hou, T. Ni, J. Zhou, C. Zhang, K. Tong, S. Dai, L. Chu, H. Wang and M. Huang, *ACS Nano*, 2025, **19**, 39839-39852.
- 190 Y. He, F. Yan, X. Zhang, C. Zhu, Y. Zhao, B. Geng, S. Chou, Y. Xie and Y. Chen, *Adv. Energy Mater.*, 2023, **13**, 2204177.
- 191 C. Zhao, J. Wang, Y. Gao, J. Zhang, C. Huang, Q. Shi, S. Mu, Q. Xiao, S. Huo, Z. Xia, J. Zhang, X. Lu and Y. Zhao, *Adv. Funct. Mater.*, 2023, **34**, 2307917.
- 192 J. Zhao, J. Wang, J. Yao, L. Li, D. Chen, G. Li and G. Zhang, *Angew. Chem. Int. Ed.*, 2025, **64**, e202505031.
- 193 Y. Fan, J. Zhao, J. Zhou, W.-H. Huang, J. Zhu, C.-Y. Kuo, S. Zhang, C.-W. Pao, T.-S. Chan, Y. Zhang, S.-Y. Hsu, J.-M. Chen, C.-T. Chen, C. Jin, L. H. Tjeng, J.-Q. Wang, Z. Hu and L. Zhang, *Energy Environ. Sci.*, 2025, **18**, 7527-7540.
- 194 D. Miao, J. Li, J. Ren and Z. Chen, *Adv. Mater.*, 2026, **38**, e20491.
- 195 Q. Xu, L. Zhang, J. Zhang, J. Wang, Y. Hu, H. Jiang and C. Li, *EnergyChem*, 2022, **4**, 100087.
- 196 H. Zhang, J. Wang, J. Yao, Q. Yang, X. Zuo, H. Tang, W. Wang, L. Yang and G. Li, *Angew. Chem. Int. Ed.*, 2025, **64**, e202506563.
- 197 S. Jeong, U. Kim, S. Lee, Y. Zhang, E. Son, K.-J. Choi, Y.-K. Han, J. M. Baik and H. Park, *ACS Nano*, 2024, **18**, 7558-7569.
- 198 J. Xu, M. Zhong, X. Chen, C. Wang and X. Lu, *Sep. Purif. Technol.*, 2023, **320**, 124184.
- 199 D. Kong, C. Meng, Y. Wan, N. Wang, Y. Zhou, Y. Zhang, M. Huang, X. Zhang, B. Wang, M. Wu, L. Wang and H. Hu, *Angew. Chem. Int. Ed.*, 2025, **65**, e24052.
- 200 L. Wang, M. Na, R. Du, X. Wang, B. Yu, L. Yang, H. Chen and X. Zou, *Chin. J. Catal.*, 2025, **77**, 4-19.
- 201 A. Thakur, W. J. Highland, B. C. Wyatt, J. Xu, N. Chandran B. S, B. Zhang, Z. D. Hood, S. P. Adhikari, E. Oveisi, B. Pacakova, F. Vega, J. Simon, C. Fruhling, B. Reigle, M. Asadi, P. P. Michałowski, V. M. Shalaev, A. Boltasseva, T. E. Beechem, C. Liu and B. Anasori, *Nat. Synth.*, 2025, **4**, 888-900.
- 202 M. Kim, J. Lee, C. Lee, J. Park, E. Lim, S. K. Cho and S. Lee, *Chem. Eng. J.*, 2025, **522**, 167136.
- 203 Q. Wang, Y. Chen, X. Zang, H. Li, W. Xiao, Y. Zong, G. Fu, J. Wang, Z. Wu and L. Wang, *Chem. Eng. J.*, 2025, **512**, 162421.
- 204 W. Jiang, S. L. Zhang, J. Yang, S. Hu, D. Duan, J. Z. X. Heng, Z. Wang, W. Yang, X. Liu, Q. Yan, M. Zhang, W.-Y. Wu, J. Hu, J. Li, N. Ding, S. L. Teo, C. Y. Chan, M. Lin, H. Liu, X. J. Loh, Y.-W. Zhang, Z. Liu, E. Ye, Y. Xiong and M. Zhao, *J. Am. Chem. Soc.*, 2025, **147**, 35293-35303.
- 205 H. Zhao, B. Ni, Y. Pan, Y. Li, J. Li, G. Wang, Z. Zou, K. Jiang, Q. Cheng, L. Zu and H. Yang, *Adv. Mater.*, 2025, **37**, 2503221.
- 206 C. Cheng, B. Yao, S. Wu, W. Gou, X. Luo, X. Chen, X. Zhang, H. Sun, C.-P. Li and B. Mao, *J. Energy Chem.*, 2026, **113**, 278-288.
- 207 S. Fan, R. Yao, Y. Niu, J. Yao, Y. Sun, J. Li and G. Liu, *Appl. Catal. B: Environ. Energy*, 2026, **382**, 126023.
- 208 T. Wu, S. Gao, R. Ma, R. Zhang, C. Wang, D. Guo, D. Lu, Z. Tian, M. Jiao, Z. Zhou and G. Shao, *Carbon Energy*, 2025, **8**, e70151.
- 209 Y. Liu, L. Wu, Y. Wang, L.-W. Shen, G. Tian, L. Cui, L. Qin, L. Zhou, Y. Zhang, F. Rosei and X.-Y. Yang, *ACS Nano*, 2025, **19**, 2715-2725.
- 210 L. Wang, M. Ma, C. Zhang, H. H. Chang, Y. Zhang, L. Li, H. Y. Chen and S. Peng, *Angew. Chem. Int. Ed.*, 2024, **63**, e202317220.
- 211 J. Yang, S. Yang, L. An, J. Zhu, J. Xiao, X. Zhao and D. Wang, *ACS Catal.*, 2024, **14**, 3466-3474.
- 212 Y. Feng, Y. Wei, B. Wu, J. Li, Q. Dong, X. Li, Y. Wang, Q. Liu, Q. Ma, J. Zhang, W. Li, G. Chen, J. Huang and F. Zhang, *Adv. Energy Mater.*, 2025, **15**, e03878.
- 213 X. Duan, N. Wen, S. Liu, H. Li, X. Jiao, D. Chen and Y. Xia, *ACS Catal.*, 2025, **15**, 10119-10129.



### Data availability statements

No primary research results, software or code have been included and no new data were generated or analysed as part of this review.

